Astronomy & Astrophysics manuscript no. sandin
June 24, 2014
©ESO 2014

The influence of diffuse scattered light

I. The PSF and its role to observations of the edge-on galaxy NGC 5907

Christer Sandin⋆

Leibniz-Institut für Astrophysik Potsdam (AIP), An der Sternwarte 16, 144 82 Potsdam, Germany

Received 15 January 2014 / Accepted 12 June 2014

ABSTRACT

All telescopes and instruments are to some degree affected by scattered light. It is possible to estimate the amount of such scattered light, and even correct for it, with a radially extended point spread function (PSF). The outer parts of the PSF have only rarely been determined, since they are faint and therefore difficult to measure. A mostly complete overview of existing properties and measurements of radially extended PSFs is presented, to both show their similarities and to indicate how bright extended objects can be used to measure the faintest regions. The importance of the far wings of the PSF and their possible temporal variations are demonstrated in three edge-on galaxy models. The same study is applied to the first edge-on galaxy where earlier observations reveal a halo, NGC 5907. All PSFs were collected in two diagrams, after they were offset or normalized, when that was possible. Surface-brightness structures of edge-on galaxies were modelled and analysed to study scattered-light haloes that result with an exponential disc. The models were convolved with both a lower-limit PSF and a more average PSF. The PSF of the observed data could be used in the case of NGC 5907. The comparison of the PSFs demonstrates a lower-limit r^{-2} power-law decline at larger radii. The analysis of the galaxy models shows that also the outer parts of the PSF are important to correctly model and analyse observations and, in particular, fainter regions. The reassessed analysis of the earlier measurements of NGC 5907 reveals an explanation for the faint halo in scattered light, within the quoted level of accuracy.

Key words. methods: data analysis – methods: observational – galaxies: halos – galaxies: structure – galaxies: individual: NGC 5907 – telescopes

arXiv:1406.5508v1 [astro-ph.GA] 20 Jun 2014

1. Introduction

Optical parts of telescopes, instruments, and detectors, as well as the atmosphere, give rise to scattered light. Imaging theory defines a point spread function (PSF) that describes how the light of a point source is affected by various optical scattering effects within these parts. The projected surface brightness structure of an object is convolved with the PSF to form the observed structure. The time-variable and field-dependent PSF, moreover, extends to large angular radii. Whilst the PSF rapidly becomes faint with increasing radii, the integrated amount of light in its faint extended wings can still be significant. If not corrected for, the scattered light adds a systematic component to observed intensities, where the amplitude, the shape, and its influence on data are unclear.

Various astronomical studies examine, to different depths of detail, how scattered light influences their analysis. The first studies address large elliptical galaxies (de Vaucouleurs 1948, 1953), M 31 (de Vaucouleurs 1958), and NGC 3379 (de Vaucouleurs & Capaccioli 1979; Capaccioli & de Vaucouleurs 1983, hereafter CV83); in these cases effects of scattered light are small. Corresponding effects on envelopes of supergiant elliptical (cD) galaxies appear to be small as well (Mackie 1992); however, the light profile in the outer regions of A 2029 closely follows the standard elliptical-galaxies de Vaucouleur's law (Uson et al. 1991), but only after they carefully remove extended and diffuse scattered-light components of field stars.

To isolate effects on colours, it is necessary to consider possible variations of the PSF with the wavelength. One study of 36 elliptical and lenticular galaxies convolve data of one bandpass with the PSF of the second bandpass before calculating colours (Idiart et al. 2002); the study, however, provides no information on how this method compares with a deconvolution in the separate bandpasses. The combined effects of colours and temporal variations of scattered light are at first studied in observations of four elliptical-type galaxies (Michard 2002); this important study reports smaller effects in the two larger galaxies NGC 4406 and NGC 4473, whilst the two smaller galaxies NGC 4550 and NGC 4551 show larger effects.

Observations of extended emission around much brighter point sources are easily corrected through the use of a scaled PSF. Several studies subtract substantial amounts of scattered light from the central-star component in observations of circumstellar shells around old giant stars (Bernat & Lambert 1975; Mauron & Caux 1992; Plez & Lambert 1994; Gustafsson et al. 1997; González Delgado et al. 2001). Observations of hosts of distant quasi-stellar objects are also corrected by subtracting emission that originates in one or a few bright components that appear as point sources (Rönnback et al. 1996; Wisotzki et al. 2002; Örndahl et al. 2003). Extended and faint ionized haloes around planetary nebulae (PNe) are affected by scattered light from the drastically brighter central parts (Middlemass et al. 1989); the authors do not measure a PSF by themselves, but analyse their data of BD+30°3639 with the extended PSF of King (1971, hereafter K71). Other studies search deep exposures of PNe for additional haloes (e.g., Corradi et al. 2003), focusing on observations that

⋆ E-mail: CSandin@aip.de

show clumps and asymmetries, and avoiding data that only show diffuse light. With few exceptions these studies do not derive any physical properties of the haloes. One bold spectroscopic study, so far, both addresses scattered light and aims to measure physical properties in PN haloes (Sandin et al. 2008); the goal of this study was to derive the mass-loss evolution of the previous phase on the asymptotic giant branch with the PN halo data.

De Jong (2008, hereafter J08) makes a more detailed study of the influence of scattered light on observations of smaller edge-on galaxies, both with data in the *Hubble* Ultra Deep Field (Beckwith et al. 2006) of the *Hubble* Space Telescope (*HST*) and in stacked data of the ground-based Sloan Digital Sky Survey (SDSS). He argues that PSF effects nearly fully explain *HST* data, but effects are smaller in SDSS data (accounting for 20–80 per cent of the halo light) and merely inner regions are affected. He dismisses its role in larger objects by their size, because he assumes a too steep slope at large radii (see below). Tziamtzis et al. (2009) set out to study density profiles in the halo outside a shock front around the supernova remnant of the Crab nebula, but because of high levels of scattered light, this was unattainable. Bergvall et al. (2010) make a case to dismiss scattered light as a general phenomenon in a simplified study of stacked SDSS images of low surface-brightness edge-on galaxies. The most recent study I mention is that of Feldmeier et al. (2013), who make a serious effort to account for effects of scattered light in a search for haloes around Lyα emitting galaxies; they find that haloes at redshift $z \simeq 2.1$ can be fully explained by scattered light, whilst small haloes of galaxies at redshift $z \simeq 3.1$ are partly still present after the scattered light is removed.

The cases that are mentioned above cannot be more than examples, as how scattered light is treated is nearly always part of the methods, and not a main topic. With few exceptions, studies that claim they address the role of scattered light only focus on measuring one PSF for all data, which is scaled to see how it matches object intensity structures of largely different origins. This procedure is ineffective with extended objects, where it is necessary to deconvolve surface-brightness structures with the PSF at the time of the observations. The few studies that deconvolve their data rarely consider temporal variations in the outer parts of the PSF, or they underestimate or truncate the PSF at some radius. The extended PSF is central to the analysis of scattered light, but it is unclear how it varies with wavelength, time, and location. And the faint outer wings are poorly known, partly since there is no established procedure to measure them.

This study focuses on ground-based observations in the visual wavelength range, 300–900nm. I begin with an overview of measured radially extended PSFs in Sect. 2, providing an update of the studies of K71 and Bernstein (2007, hereafter B07). The overview focuses on two aspects that were not accounted for in any detail before. Measurements of the encircled energy show that the far regions of the PSF may contribute significant amounts of light. Current measurements of PSFs only measure stars; I demonstrate how planets, the Moon, and the Sun, can be used at larger radii instead, as in earlier studies. The analysis method that is used to model surface-brightness structures of edge-on galaxies is described in Sect. 3. Example models of a small, an intermediate size, and a large edge-on disc galaxy are also analysed here; these examples demonstrate the decisive importance of using PSFs that are not truncated at short radii.

As an example of a real object, I analyse models and measurements of the edge-on galaxy NGC 5907 in Sect. 4. This is an important object, since it presents the first case where a halo of excess light was found around an edge-on galaxy (Sackett et al. 1994). I reassessed the analysis of Morrison et al. (1994, hereafter MBH94), to show that it is possible to explain both the halo and the red excess in the halo by scattered light. The paper is finished with a brief discussion and conclusions in Sect. 5.

2. Measurements and properties of the PSF

In the formalism of imaging theory the PSF describes how a point-source image is affected by broadening through detector effects, optical aberrations, diffraction, and scattering effects within the instrument, the telescope, and the atmosphere. The shape of the PSF is determined by atmospheric turbulence in the bright centre region, where it can be described by a Moffat profile, using Kolmogorov statistics (Racine 1996). The much fainter region outside the centre, the so-called aureole, is less well understood and has been a target for scrutiny. Possible sources of the aureole include scattering by atmospheric aerosols and dust, as well as micro-ripples and dust on optical surfaces (for example, van de Hulst 1948; Deirmendjian 1957, 1959), and effects of diffusion and reflection within the instrument (Hasan & Burrows 1995; Racine 1996; B07; Slater et al. 2009, hereafter SHM09). The aureole eventually, at say 1°.5, merges into an extremely faint 'blue-sky' component of Rayleigh scattering that extends to, say, 90° (Deirmendjian 1957, 1959).

I begin with an overview and comparison of empirically measured radially extended PSFs in Sect. 2.1. The PSF comparison of B07 is discussed separately in Sect. 2.2. Thereafter, I describe how the PSFs are normalized and extrapolated to larger radii in Sect. 2.3, and discuss the outcome of measurements of the encircled energy in Sect. 2.4. Guidelines on how to make new PSF measurements are provided in Sect. 2.5. Only instrument and telescope effects remain outside of the Earth atmosphere. A brief outline to how *HST* data could also be affected by radially extended PSFs is presented for completeness in Sect. A.

2.1. An overview of measured radially extended PSFs

Few PSFs are measured out to large angles (radii r). Here I overview a sample of PSFs that were measured with different instruments and filters, at various telescopes, to show their similarities in terms of shape and radial extent. Most PSFs are shown in Fig. 1, where they are normalized to 0 mag; the PSFs that are discussed in Sect. 2.2 are shown separately in Fig. 2, to avoid that Fig. 1 is overfilled. Information of observational setups and radial extents of all discussed PSFs are collected in Table 1.

K71 presents the radially extended $\mathrm{PSF_{K71}}$ that continues out to $r \simeq 5°$; this PSF is a composite of his own measurements with the 48" telescope at the Palomar Observatory and, amongst other, the measurements of de Vaucouleurs (1958), who used the 21" reflector at the Lowell Observatory. Kormendy (1973) presents $\mathrm{PSF_{K73}}$ for the radial range $7'' \leq r \leq 1°$, which was also measured with the 48" telescope at Palomar. With $\mathrm{PSF_{CV}}$, CV83 present the, so far, radially most extended PSF, which reaches $r = 90°$ and covers more than 30 mag in intensity. When CV83 measure $\mathrm{PSF_{CV}}$, they simplify their analysis and assume that the PSF is well fitted by a sum of three Gaussian profiles (this approach is earlier also used by de Vaucouleurs 1948; Brown 1978). Their analysis on the origin of the PSF and various sources of errors is thorough, but it is applied to NGC 3379, which is an extended elliptical galaxy with a slowly decreasing surface brightness; they show that in this case the PSF is of minor importance. $\mathrm{PSF_{CV,1}}$ and $\mathrm{PSF_{CV,2}}$, which only differ in the core, are claimed to be measured at a seeing of 0".5 and 1".0, respectively, instead of the real values 1".0 and 2".0 that can be measured in the profiles.

Table 1. Chronological list of measurements of radially extended PSFs.

PSF	Fig.	Ref.	Observatory	Alt.	Telescope	Band / Line	Range	Object (Symbol)
PSF_{K71}	1, 2	1–4	Solar Physics	30	36" Common reflector	...	~ 20″–180″	stars
	1	2–4				...	1′, 4′	⊙ (△)
	1, 2	3, 4	Lowell	2195	21" reflector	*B*	~ 20″–5°	♃ and 2m star
	1, 2	4	Palomar	1713	48" Schmidt	*B*	1.″3–228″	stars (●, ×)
	1, 2		Mount Wilson	1742	60" reflector	*B*	–5.″6	3 stars (○)
PSF_{K73}	1, 2	5	Palomar	1713	48" Schmidt	*B*	7″–1°	stars
PSF_{P73}	1	6	Goethe Link	293	16" reflector	*B*	48″–170′	stars, ☾ (○, ●, ▲)
			McDonald	2076	2.1m Otto Struve	...	not shown	
PSF_{S74}	2	7	Palomar	1713	48" Schmidt	RG-1	100–600″	stars (▲)
PSF_{CV},		8	McDonald	2076	0.9m	*B*	10″–4.″6	γCMa
($PSF_{CV,1}$,	1					...	3.5–90′	αCMa
$PSF_{CV,2}$)	1, 2					...	1.5–90°	⊙
PSF_{S90}	2	9	Calar Alto	2168	1.23m	*R*	≲ 480″	stars (□)
PSF_{U91}	2	10	Kitt Peak	2160	1.09m	*R*	1–975″	stars
PSF_{M92}	2	11	Kitt Peak	2160	24/36" B. Schmidt	*g*	5–92″	HD 19445 (●)
PSF_{MBH}	1	12	Kitt Peak	2160	No. 1 0.9m (SARA)	Harris *R*	0–150″	two stars
PSF^{new}_{MBH}	1							
$PSF_{V,0m}$,	1, 2	13	Haute Provence	650	1.2m Newtonian	*V*	≲ 160″	stars
$PSF_{V,3m}$	1							
$PSF_{i,0m}$,	1, 2					*I*	≲ 160″	stars
$PSF_{i,3m}$	1							
PSF_{G05}	2	14	Las Campanas	2282	40" Swope	Gunn *i*	10–400″	stars
PSF_{B07}	2	15	Las Campanas	2282	100" Du Pont	*r*	≲ 400″	stars
$PSF_{P,LR}$	1	16	Calar Alto	2168	3.5m / PMAS	Hα	–25″	αLyr
PSF_{S09}	1	17	Kitt Peak	2160	24/36" B. Schmidt	Wash. *M*	1.″4–64′	αBoo, star
SDSS	1	18, 19, 20, 21	Apache Point	2788	2.5m	*g*, *r*, *i*, ...	≲ 46″	stars
PSF_{A14}	1	22	New Mexico Skies	2200	Dragonfly Array	*r*	5.″1–56.′8	αLyr

Notes. Column. 1, PSF notation used in this paper; Col. 2, the PSF is shown in this figure; Col. 3, references; Col. 4, observatory; Col. 5, altitude of the observatory (m); Col. 6, telescope (/instrument); Col. 7, wavelength bandpass or line that was used; Col. 8; radial extent of PSF measurements; and Col. 9, objects used to measure the PSF (and symbols used in Fig. 1). The object symbols are ♃ (Jupiter), ☾ (the Moon), and ⊙ (the Sun).

References. (1) Redman & Shirley (1938); (2) van de Hulst (1948); (3) de Vaucouleurs (1958); (4) K71; (5) Kormendy (1973); (6) Piccirillo (1973); (7) Shectman (1974); (8) CV83; (9) Surma et al. (1990); (10) Uson et al. (1991), (11) Mackie (1992); (12) MBH94; (13) Michard (2002); (14) Gonzalez et al. (2005); (15) B07; (16) Sandin et al. (2008); (17) SHM09; (18) Zibetti et al. (2004); (19) J08; (20) Bergvall et al. (2010); (21) Tal & van Dokkum (2011); (22) Abraham & van Dokkum (2014) .

Sandin et al. (2008) measure a spectroscopy PSF using the lens array integral field unit of the Potsdam Multi Aperture Spectrograph (PMAS). The published PSF was measured using saturated data, which resulted in a too wide core profile. Here, $PSF_{P,LR}$ is presented, where the core profile is replaced with the PSF of a faint star that was observed at 0.″8 seeing (this procedure causes the kink in $PSF_{P,LR}$ that is seen at $r \approx 1.''5$). $PSF_{P,LR}$ only extends to $r \simeq 25''$, but it agrees well with the imaging PSFs – this indicates that PSF effects are plausibly equally critical in imaging and spectroscopy data. Monreal-Ibero et al. (2006) show the only other example of an extended spectroscopy PSF that I know of, for the VIsual Multi-Object Spectrograph at the Very Large Telescope, but it only reaches $r = 12''$. Moreover, SHM09 study the instrumental origin of the PSF and present the composite PSF_{S09}, which extends to $r \simeq 64'$. These authors show that the aureole brightness depends strongly on where measurements are made in the field. Measurements that are offset from the optical axis may, depending on the amplitude of the offset and changing optical conditions, result in asymmetric PSFs.

The PSF studies that were mentioned so far do not examine any time or wavelength variations outside the centre PSF. Such variations are since long found in photometer measurements near the solar limb (Michard 1953; Pierce 1954) and off the bright limb of the Moon (Piccirillo 1973); the latter study presents three sections of the aureole with PSF_{P73}. Piccirillo, moreover, finds a correlation between the measured aureole and times of mirror re-aluminizing and washing, as well as the telescope location. The aureole that he measures with data from the McDonald Observatory (not published) is time invariant, whilst the one that he measures at the Goethe Link Observatory increases by up to a factor ten within a few months. Michard (2002) measures inner aureoles at the Haute-Provence Observatory with various imaging filters that also show temporal changes. He presents the only published radially extended PSFs that are available for two bands at two distinct times (they are separated by three months; $PSF_{V,0m}$, $PSF_{V,3m}$, $PSF_{i,0m}$, and $PSF_{i,3m}$). The two *V*-band PSFs differ by up to 1 mag arcsec^{-2}, whilst the two *i*-band PSFs show a smaller difference. In general, PSFs show weak variations with wavelength, except measurements in the *i*-band that in some parts are affected by the CCD-specific red halo effect (Sirianni et al. 1998). PSF_{K71}, PSF_{K73}, PSF_{P73}, and PSF_{CV} (as well as PSF_{S74}, see Sect. 2.2) were measured with photographic and photomultiplier data, and more recent PSFs with CCDs.

Several studies stack a large number of images of the Sloan Digital Sky Survey (SDSS) and then measure one PSF per band; for example, Zibetti et al. 2004, J08, Bergvall et al. 2010, and

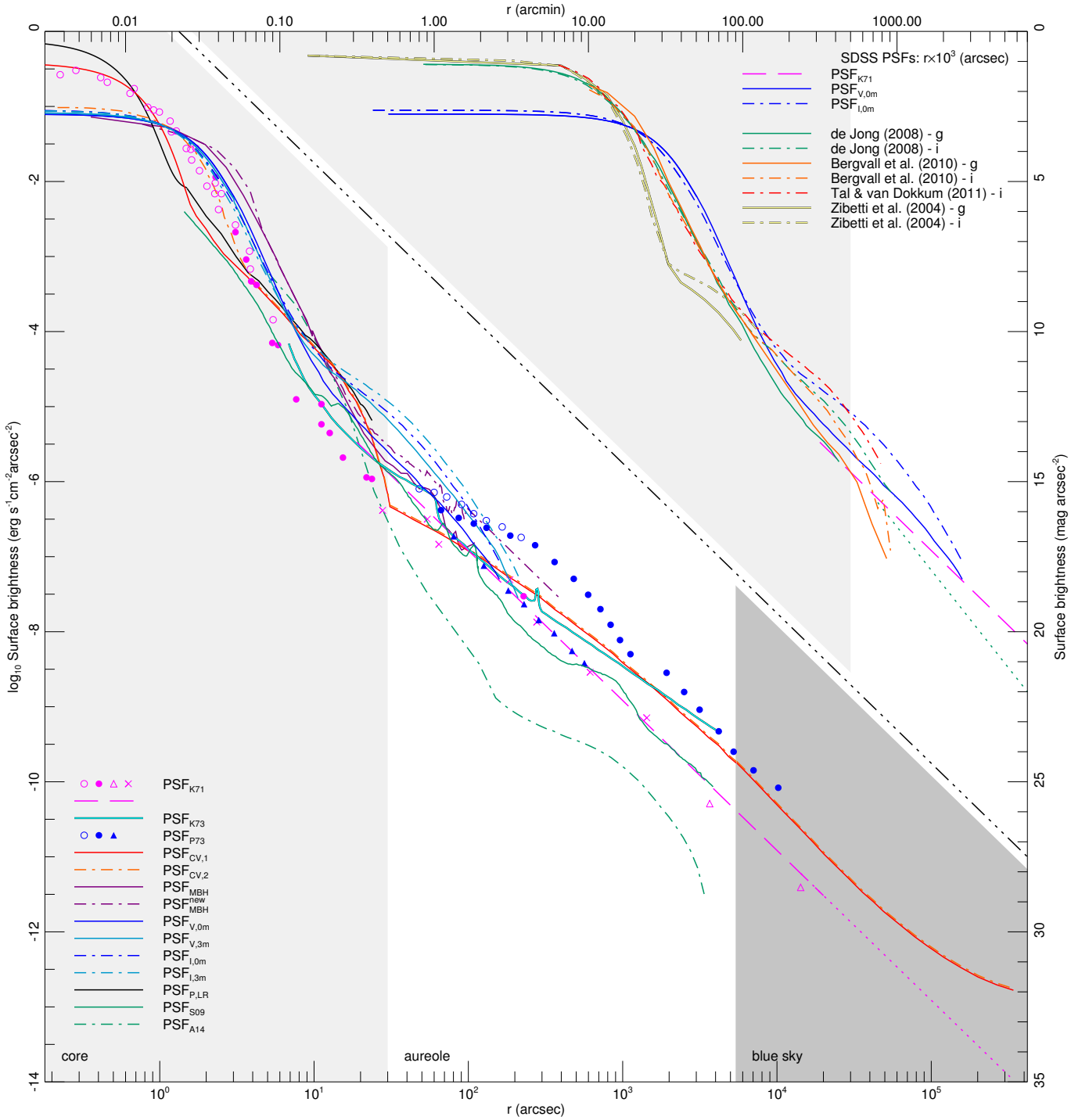

Fig. 1. PSF surface-brightness profiles versus the radius r for a 0 mag point source. Individual PSFs are drawn with coloured lines and symbols as indicated in the figure, also see Table 1. PSFs of stacked SDSS images are shown in the upper part of the figure, as function of $10^3 \times r$; $\mathrm{PSF}_{V,0\mathrm{m}}$, $\mathrm{PSF}_{i,0\mathrm{m}}$, and the outer regions of $\mathrm{PSF}_{\mathrm{K71}}$ are shown in both parts as references. Extrapolated PSFs are shown with dotted lines. The light (medium) grey region indicates the PSF core (blue sky) and the white region the aureole, as defined for $\mathrm{PSF}_{\mathrm{CV},1}$ and $\mathrm{PSF}_{\mathrm{CV},2}$ (CV83).

Tal & van Dokkum 2011, which extend to $r \simeq 30$–$60''$. The g- and i-band SDSS PSFs are shown in Fig. 1 versus $10^3 \times r$, separated from the other PSFs. J08 extrapolates his PSF for $r > 71''$, using a $r^{-2.6}$ power law (dotted dark green line in Fig. 1). This extrapolation is poorly justified in comparison with, for example, $\mathrm{PSF}_{\mathrm{K71}}$ and $\mathrm{PSF}_{\mathrm{S09}}$, which decline as r^{-2}, and other PSFs are even more shallow [$\mathrm{PSF}_{\mathrm{P73}}$(∘, •), $\mathrm{PSF}_{\mathrm{K73}}$, and $\mathrm{PSF}_{\mathrm{CV}}$]. The SDSS PSFs are all averaged using a large number of 53 s exposures that were collected during years of observations. Such PSFs, of individual filters, should be nearly identical, if they are time invariable and differences across the field are ignored. Figure 1 shows that the i-band filter PSFs differ by up to two magnitudes, in particular the i-band PSF of Tal & van Dokkum (2011) lies above the other ones. The large deviation between the PSFs in the outermost parts illustrates that the SDSS exposure time of 53 s might be too short for these measurements. It is plausible that the SDSS PSFs are affected by either temporal variations, optical-path differences across the field, or both.

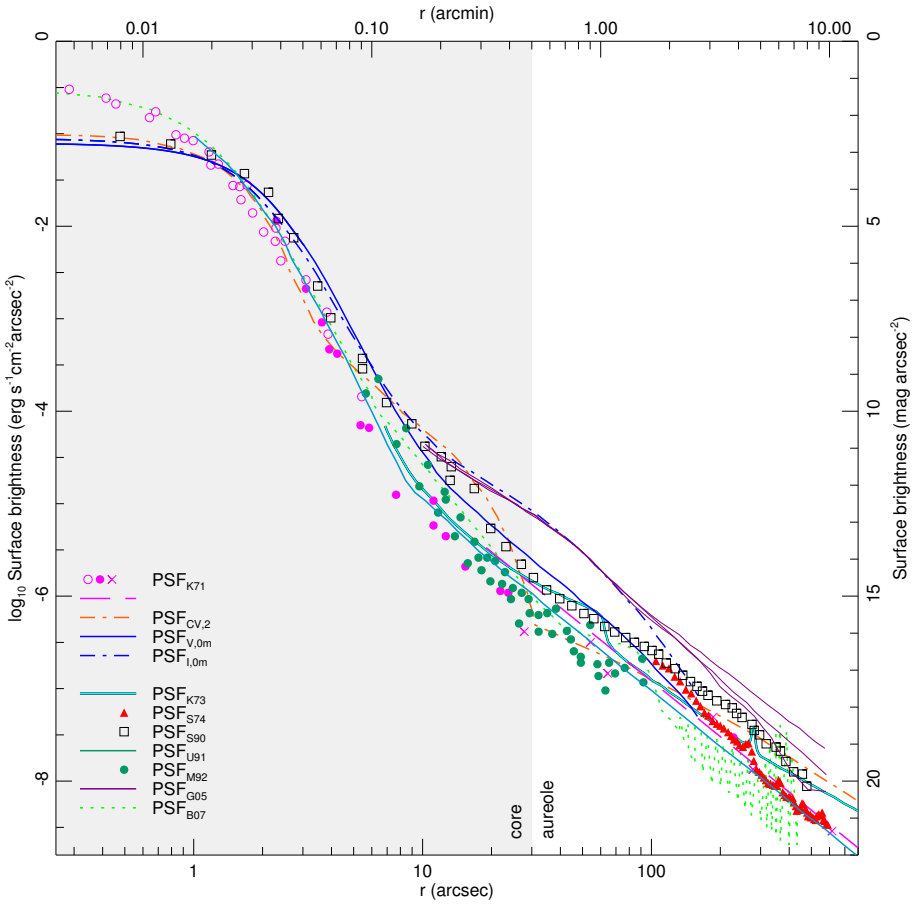

Fig. 2. PSF surface-brightness profiles versus the radius r for a 0 mag point source, from references that are discussed by B07. Individual PSFs are drawn with coloured lines and symbols as indicated in the figure, also see Table 1. $\mathrm{PSF_{K71}}$, $\mathrm{PSF_{\mathit{V},0m}}$, $\mathrm{PSF_{\mathit{i},0m}}$, and $\mathrm{PSF_{CV,2}}$ are shown in this figure as references. The light grey region indicates the PSF core, and the white region the aureole, as defined for $\mathrm{PSF_{CV,1}}$ and $\mathrm{PSF_{CV,2}}$ (CV83).

Two of the three remaining PSFs in Fig. 1 are $\mathrm{PSF_{MBH}}$ and $\mathrm{PSF^{new}_{MBH}}$. MBH94 present $\mathrm{PSF_{MBH}}$ in their analysis of NGC 5907 and $\mathrm{PSF^{new}_{MBH}}$ is derived here, both PSFs are discussed further in Sect. 4.

Most of the PSFs mentioned here are measured with telescopes that use reflective mirrors; remaining parts use scaled intensity estimates of the sky away from the sun. Abraham & van Dokkum (2014) instead use an optical configuration with eight, comparatively small, refracting telephoto lenses. Their resulting $\mathrm{PSF_{A14}}$ lies markedly lower than all other PSFs where $r \gtrsim 30''$.

The presented PSFs clearly illustrate that there is no empirical support for truncating a PSF at a shorter radius. Except in the innermost seeing-dependent core, and where $100 \lesssim r \lesssim 400''$, $\mathrm{PSF_{K71}}$ appears to present an approximative lower limit of the extent of scattered light throughout the radial range in reflective telescopes. Except $\mathrm{PSF_{S09}}$ and $\mathrm{PSF_{A14}}$, the outer PSF (where $r \gtrsim 500''$) was measured once in the early eighties ($\mathrm{PSF_{CV}}$), and only thrice before that ($\mathrm{PSF_{K71}}$, $\mathrm{PSF_{K73}}$, and $\mathrm{PSF_{P73}}$). Additionally, Wu et al. (2002) claim that they measured a PSF that extends to $r = 1700''$, but they do not present it (and the data are lost, Wu, priv. comm.). I speculate that the r^{-2} dependence at large radii of the other PSFs, at least partially, occurs due to an obstructed pupil and reflective surfaces, whilst PSFs that are even brighter occur due to the degradation of, as well as deposition of dust, on reflective optical surfaces.

2.2. Further evidence against a steeper than r^{-2} power-law slope that contradicts the conclusion of B07

B07 discusses PSFs from the viewpoint of their slope at different radii. She notes that the slopes of the outer PSF differ, which are measured with the 48" telescope at Palomar by three different authors. To this purpose, she compares the r^{-2} slope of K71 for $r < 228''$ (the exact dates of these measurements are not specified) with the $r^{-1.7}$ slope of Kormendy (1973, measured August 1971–April 1972) for $3 \leq r \leq 30'$, and the $r^{-2.6}$ slope of Shectman (1974, measured March–April 1971) for $r = 100''$, and summarizes that the PSF of this telescope is not well determined within a time frame of a few months. She notes that differences are probably the result of filter and emulsion use, mirror cleanliness, and measurement errors. In view of the two sets of PSFs of Michard (2002), it seems plausible that the temporal resolution of the Palomar PSFs is too poor to draw any conclusion about how the PSFs change with time. Note, however, that the feature at $r \approx 280''$ is seen in both $\mathrm{PSF_{K73}}$ and $\mathrm{PSF_{S74}}$.

The comparison of slopes that B07 presents appears less dramatic when all PSFs are collected in the same plot. All but one PSF of B07 are shown in Fig. 2. The exception are the data of Middlemass et al. (1989), who use $\mathrm{PSF_{K71}}$ and present data of the small, but extended, planetary nebula BD+30°3639 (in their fig. 1); B07 seemingly uses these data as a PSF. B07 measures $\mathrm{PSF_{B07}}$ that reaches $r \simeq 400''$, and is centred on the optical axis. She also measures a second PSF that is offset by $3'$ from the optical axis; in view of the lack of details regarding the optical setup, and with respect to the discussion and results of SHM09, it is uncertain how the offset PSF can be compared to $\mathrm{PSF_{B07}}$. For example, on which side of the optical axis is the offset PSF measured? Whilst there are local deviations from a slope that decreases as r^{-2}, there is no evidence for a globally steeper slope in telescopes that use reflective mirrors, neither in Fig. 2 nor in Fig. 1. $\mathrm{PSF_{B07}}$ is partly lower in the outermost regions, where it is also very noisy.

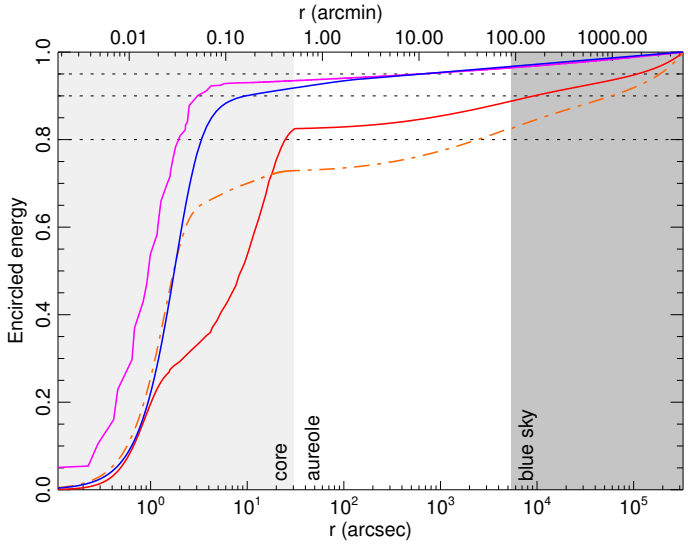

Fig. 3. Encircled energy versus the radius r. The four shown PSFs are: $\mathrm{PSF_{K71}}$ (magenta, uppermost line), $\mathrm{PSF_{CV,1}}$ (red, lowermost line for $r < 20''$), $\mathrm{PSF_{CV,2}}$ (orange, lowermost dash-dotted line for $r > 20''$), and $\mathrm{PSF_{V,0m}}$ (blue). The light (medium) grey region indicates the PSF core (blue sky), and the white region the aureole, as defined for $\mathrm{PSF_{CV,1}}$ and $\mathrm{PSF_{CV,2}}$ (CV83). The horizontal dotted lines at 0.8, 0.9, and 0.95 are guides.

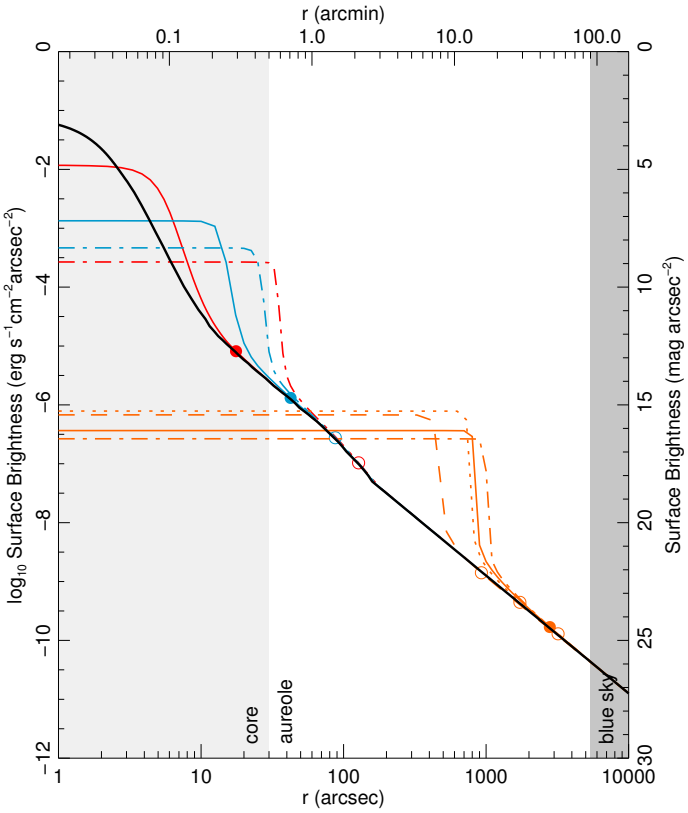

Fig. 4. Comparison of $\mathrm{PSF_{V,0m}}$ (black line) with surface-brightness profile cuts of Venus (red lines), Jupiter (blue lines), the full Moon (orange solid and dash-dotted lines), and the half Moon on the symmetry axis (orange dashed line) and the axis orthogonal to that (orange dotted line). Profiles of objects at apogee (perigee) are drawn with solid (dash-dotted) lines. All profiles, but $\mathrm{PSF_{V,0m}}$, were divided with the illuminated area of the respective object. The light (medium) grey region indicates the PSF core (blue sky), and the white region the aureole. Bullets and circles indicate r_{PSF} of individual profiles, cf. Table 2.

2.3. Extrapolating and normalizing the PSFs

I chose to normalize all PSFs that are measured near the centre to $r = 90°$, which is the largest radius that was considered in the derivation of a PSF (see the information on $\mathrm{PSF_{CV}}$). Even larger radii cannot be excluded. In the centre region, I extrapolated each PSF to $r = 0$ with centred and fitted Gaussian profiles. All details of the normalization and extrapolation to larger radii of individual PSFs are given in Sect. B.

The outer regions of the PSFs are only poorly known, at best, which makes the normalization uncertain. In this paper, I delimited the study of objects to the radial range $r < 450''$, and use PSFs in the radial range $r < 900''$ (cf. Sect. 3.4).

2.4. Measuring the encircled energy

Whilst the radially extended PSF may reach $r = 90°$, and beyond, only the inner parts, which are induced by the instrument and not the atmosphere, are expected to affect the accuracy of flux measurements (CV83; B07). CV83 measure the B-band $\mathrm{PSF_{CV}}$ and find that the energy fraction in the aureole and the blue sky, 30 per cent, corresponds to the atmospheric extinction in the B-band. To check how general this finding is, the encircled energy is shown versus radius for four PSFs in Fig. 3: $\mathrm{PSF_{CV,1}}$ and $\mathrm{PSF_{CV,2}}$, which share the outer profile, and $\mathrm{PSF_{K71}}$ and $\mathrm{PSF_{V,0m}}$. About 28 per cent of the encircled energy is contained in the aureole and the blue sky parts of $\mathrm{PSF_{CV,2}}$, in agreement with CV83. However, the value is about 18 (6.5; 8) per cent for $\mathrm{PSF_{CV,1}}$ (B-band $\mathrm{PSF_{K71}}$; V-band $\mathrm{PSF_{V,0m}}$). Also, the outer parts of $\mathrm{PSF_{CV}}$ were measured without any filter (Table 1). $\mathrm{PSF_{CV}}$ (and thereby $\mathrm{PSF_{CV,1}}$ and $\mathrm{PSF_{CV,2}}$) becomes more shallow for $r \gtrsim 1000'$, possibly as a result of fitting the measurements with three Gaussian profiles. The shallower PSF causes slopes that are steeper than those of $\mathrm{PSF_{K71}}$ and $\mathrm{PSF_{V,0m}}$ in the outermost (blue-sky) region, cf. Fig. 3.

Considering the quoted percentages and that the extinction decreases for redder wavelengths, with the currently measured PSFs there is clearly no simple correlation between the fraction of energy in the outer PSF and the atmospheric extinction.

2.5. Recommendations for new measurements of the PSF

The total number of measured PSFs that extend beyond a few minutes of arc is small; $\mathrm{PSF_{K71}}$, $\mathrm{PSF_{K73}}$, $\mathrm{PSF_{P73}}$, $\mathrm{PSF_{CV}}$, and $\mathrm{PSF_{S09}}$ extend this far. Only $\mathrm{PSF_{S09}}$ was measured recently. Neither a wavelength dependence nor temporal variations were considered in the measurements of the outer parts of these PSFs; the general application of these static PSFs to deconvolve data is discouraged. It is also important that all flux is included in the calculation of azimuthally averaged profiles; the PSF is somewhat underestimated, if, for example, diffraction spikes are masked (this is measured here for the case of NGC 5907, cf. Sect. 4.2).

Nowadays, PSFs are exclusively measured using combined data of faint and bright stars. Measurements in different radial regions are combined by matching them in overlapping regions. Faint stars are used to measure the seeing-dependent core, and bright stars are used to determine the fainter outer regions. Very bright stars are, unfortunately, limited in number. Even if a bright star is used, the surface brightness cannot be accurately measured beyond some radius with reasonable exposure times (say, shorter than about 1800 s).

Table 2. Properties of the Sun, the Moon, and the brightest planets and stars on the sky.

Object	Diameter		m_V (mag)		r_{PSF} / Decl.		Comment
	apogee	perigee	max	min	apogee	perigee	
the Sun	31′.6	32′.7	−26.45		50′	52′	
the Moon	29′	34′	−2.5	−12.9	47′	54′	The full Moon
Venus	9′.7	66″	−3.8	−4.9	17″	130″	Crescent at perigee
Mars	3′.5	25′.1	+1.6	−3.0	13″	40″	
Jupiter	29′.8	50′.1	−1.6	−2.94	43″	88″	
Saturn	14′.5	20′.1	+1.47	−0.24	13″	36″	Ignoring the rings.
αCMa			−1.47		−16°42′58″		Sirius A
αCar			−0.72		−52°41′44″		Canopus
αCen			−0.27		−60°50′02″		Alpha Centauri A+B
αBoo			−0.04		+19°10′56″		Arcturus
αLyr			+0.03		+38°47′01″		Vega
αAur			+0.03–0.16		+45°59′53″		Capella

Notes. Column. 1, object name; Cols. 2 and 3, object diameter at apogee and perigee; Cols. 4 and 5, minimum and maximum V-band magnitude for planets and solar system bodies, and total magnitude for the stars; Cols. 6 and 7, minimum and maximum values on r_{PSF} using $PSF_{V,0m}$ for the Sun, the Moon, and the planets, and declination for the stars; and Col. 8, additional comments. Only approximate values on the diameters, magnitudes, and coordinates are presented here (see any book on planetary science).

Earlier PSF studies also make use of observations of Jupiter, the Moon, and even the Sun. Compared to centres of stars, surface brightnesses of the planets and the Moon are lower, but integrated intensities can be drastically higher.

Extended objects are not directly comparable to point sources. However, they appear as point sources, beginning at a geometry-dependent angular distance r_{PSF}, after they are normalized with the illuminated surface area (including a correction for intensity variations across the surface). To illustrate this, I made the simplifying assumption that each extended object is a disc of specified diameter with a constant (homogeneous) brightness. Each surface-brightness structure was convolved with $PSF_{V,0m}$ and the result was divided with the illuminated area. With the smaller planets (the larger planets; the Moon and the Sun) I created model images where I used pixels that are 0′.55 (2′.5; 10′) on the side. Surface-brightness profile cuts at the apogee and the perigee of Venus, Jupiter, and the Moon are compared with $PSF_{V,0m}$ in Fig. 4.

Object diameters at perigee and apogee, as well as magnitudes of the Sun, the Moon, the brighter planets, and the six brightest stars are collected in Table 2. Approximate values on magnitudes and sizes should suffice in this context – real PSFs are preferably derived by matching overlapping PSFs. The beginning PSF radius r_{PSF}, where the surface brightness of each respective extended object deviates by less than 5 per cent from $PSF_{V,0m}$, is shown in the same table. Adopting a generous margin, all objects appear as PSFs outside an angular radius of two times the respective object diameter, except Mars at apogee (3.7× the diameter). r_{PSF} is shown in Fig. 4 also for the half Moon at apogee, as viewed on the symmetry axis and the axis that is orthogonal to that; the corresponding beginning PSF radii are $r_{PSF} = 16'$ and $r_{PSF} = 29'$. It seems appropriate to observe other bright objects instead of the faint Mars and Saturn at their apogee, but in particular Mars is significantly brighter at perigee.

The intermediate PSF range, say $1' \lesssim r \lesssim 1°$, is well measured with Mars and Saturn at perigee, and with Venus and Jupiter at any time. De Vaucouleurs (1958) uses Jupiter to measure a PSF out to $r = 5°$, 29 mag below the integrated magnitude (these measurements are part of PSF_{K71}, cf. Table 1). B07 raises some concern that the faintest intensities measured around Jupiter are affected by Zodiacal light, but Jupiter is bright and the slope agrees with the other measurements. Venus is a crescent at perigee, the beginning PSF radius is therefore slightly smaller than what I calculated using a disc.

The outer PSF, say $1 \lesssim r \lesssim 10°$, is well measured using the bright Moon, say, when half or more of the Moon is illuminated. Krisciunas & Schaefer (1991, and references therein) provide a detailed account for issues related to measurements of the surface-brightness due to the Moon across the sky (also see Patat 2003). The outermost parts of the PSF, $1 \lesssim r \lesssim 90°$ (and beyond), could be estimated using the Sun (van de Hulst 1948, CV83). The illuminated and projected area of the Moon varies between the new Moon and the full Moon – the angular distance should be measured from the centre of mass of the illuminated area.

The edge-on galaxy models that are presented in Sect. 3.4 indicate that it is necessary to measure the PSF out to a radius that is 1.5 times larger than the measurements, to ensure that observed data can be corrected for integrated scattered light. Current measurements of PSFs are crude and few, which is why it is difficult to judge their influence on observations in general. New measurements of radially extended PSF – as function of angle, time, wavelength, and position in the field – are needed for all telescope and instrument setups that are used to observe extended objects. There are several attempts to model the outer PSF theoretically, but it is not understood how the inverse-square decline with radius is created.

Lots of observing time would be required, if it was demanded that each project observes individual PSFs. With the *HST* PSF model code TINY TIM (see the discussion on space-based PSFs in Sect. A) as an example, it seems worthwhile to explore possibilities to develop a similar tool for ground-based telescopes. Analysis work of both past and new observations could be improved if there was a PSF lookup library for different instrument modes at a telescope, as function of filter or wavelength, time, and position within the observable field. New observations could at first be made at some weekly or monthly intervals to determine the temporal variations of the PSF; it might be a good idea to also record the time since the last mirror aluminization and washing, the air quality, ground reflective properties, and the like. At the moment it seems that the extended PSF must be individually measured for each observed exposure, but the suggested approach would provide good foundations and constraints to develop the theory of the outer parts of the PSF.

3. Method and its application to example models

The simulations of the surface-brightness structure of the example galaxies and NGC 5907 were split into three steps. I selected a set of measured PSFs that can be used to estimate varying scattered-light effects. Thereafter, I configured models of the surface-brightness structure. Finally, I applied the PSFs to the model structures and analysed the outcome. These steps are described in the following three subsections. I apply the method to three example models in Sect. 3.4.

3.1. Choosing representative PSFs

Representative PSFs should describe both temporal variations and the red-halo effect in the i band, and they should extend out to $r \simeq 900''$, which is twice the maximum object radius that I consider. I chose to use the only published extended PSFs that were measured with both the (Cousins) V and the (Gunn) i bands, at two distinct occasions that were separated by three months: $\mathrm{PSF}_{V,0\mathrm{m}}$ and $\mathrm{PSF}_{i,0\mathrm{m}}$ that were measured three months before $\mathrm{PSF}_{V,3\mathrm{m}}$ and $\mathrm{PSF}_{i,3\mathrm{m}}$; the difference with radius of $\mathrm{PSF}_{V,3\mathrm{m}}-\mathrm{PSF}_{V,0\mathrm{m}}$ is on average higher than that of $\mathrm{PSF}_{i,3\mathrm{m}}-\mathrm{PSF}_{i,0\mathrm{m}}$ (Fig. 1). The comparison of the PSFs in Figs. 1 and 2 demonstrate that $\mathrm{PSF}_{V,0\mathrm{m}}$ is perhaps $\lesssim 0.5$ mag arcsec^{-2} brighter at intermediate radii than the other PSFs; the value is a bit uncertain since it was necessary to scale several PSFs. At larger radii, $r \gtrsim 80''$, it is difficult to draw such a conclusion. I used $\mathrm{PSF}_{V,0\mathrm{m}}$ as an indicator of average PSF effects with the example models in Sect. 3.4. $\mathrm{PSF}_{V,3\mathrm{m}}$ is much brighter, and is more representative of an upper limit. (See Sect. 4.2 for a comparison of $\mathrm{PSF}_{\mathrm{MBH}}$ and $\mathrm{PSF}^{\mathrm{new}}_{\mathrm{MBH}}$.) The radially extended B-band $\mathrm{PSF}_{\mathrm{K71}}$ is used as a lower limit indicator of scattered light, both with the example models and with NGC 5907. Moreover, $\mathrm{PSF}_{i,0\mathrm{m}}$ represents the i-band average SDSS PSFs well where $r \gtrsim 10''$. $\mathrm{PSF}_{i,3\mathrm{m}}$ is used as an upper limit in the i band, similar to how $\mathrm{PSF}_{V,3\mathrm{m}}$ is used. Some PSFs show more light at large radii than the r^{-2} power-law of $\mathrm{PSF}_{\mathrm{K71}}$ (see Sect. 2); the predictive ability at larger radii is therefore weaker.

In the simulations, I assumed that the two V-band $\mathrm{PSF}_{V,0\mathrm{m}}$ and $\mathrm{PSF}_{V,3\mathrm{m}}$, as well as the B-band $\mathrm{PSF}_{\mathrm{K71}}$, are the same in the R band – I do this under the assumption that measured PSFs of different bands (except the i band) are very similar, cf. Sect. 2.1. The colour predictability is delimited to $R-i$. I did not differentiate between Cousins, Harris, or other photometric systems. All five PSFs were measured at a seeing of several arc seconds, which is why the spatial resolution in the brightest centre region is poor. Here, faint diffuse emission is studied, where the spatial resolution and resulting lower intensities in the centre regions are of minor importance.

3.2. Setting up sets of model surface-brightness structures

Two-dimensional surface-brightness structures of edge-on disc galaxies are suitably described in cylindrical coordinates. The space-luminosity density I' can be described by (van der Kruit 1988; van der Kruit & Searle 1981)

$$I'(r',z') = I'_{0,0}\exp\left(-\frac{r'}{h_\mathrm{r}}\right)\times 2^{-2/n_\mathrm{s}}\mathrm{sech}^{2/n_\mathrm{s}}\left(\frac{n_\mathrm{s}z'}{z_0}\right), \quad (1)$$

where $I'_{0,0}$ is the centre intensity, r' the radius, h_r the scale length, z' the vertical distance from the centre, z_0 the vertical scale height, and n_s is set to 1, 2, or ∞. The intensity drops to zero at a galaxy-specific truncation radius. When a disc galaxy is projected edge on, and the truncation radius as well as dust extinction are ignored, the surface-brightness structure $I(r,z)$ becomes

$$I(r,z) = I_{0,0}\frac{r}{h_\mathrm{r}}K_1\left(\frac{r}{h_\mathrm{r}}\right)\times 2^{-2/n_\mathrm{s}}\mathrm{sech}^{2/n_\mathrm{s}}\left(\frac{n_\mathrm{s}z}{z_0}\right), \quad (2)$$

where $I_{0,0} = 2h_\mathrm{r}I'_{0,0}$ is the centre intensity, r the major-axis radius, z the minor-axis (vertical) distance from the centre of the disc, and K_1 the modified Bessel function of the second kind. The intensity is slightly lower at larger radii when the truncation radius is finite and taken into account; considering how uncertain the PSFs are, this effect is ignored here. I assume in Sect. 3.4 that the disc is isothermal ($n_\mathrm{s} = 2$), and in Sect. 4 it seems to work better using $n_\mathrm{s} = 1$ with NGC 5907. No attempt is otherwise made to make a perfect fit of the centre region of NGC 5907. The relation $\mu = -2.5\log_{10}(I)$ is used to convert between magnitudes μ and intensities I.

3.3. Models and measurements analysis procedure

Each two-dimensional R-band model image is convolved individually with the three resampled and normalized two-dimensional V-band $\mathrm{PSF}_{V,0\mathrm{m}}$ and $\mathrm{PSF}_{V,3\mathrm{m}}$, and the B-band $\mathrm{PSF}_{\mathrm{K71}}$. This is repeated for each i-band model image with $\mathrm{PSF}_{i,0\mathrm{m}}$ and $\mathrm{PSF}_{i,3\mathrm{m}}$. The i-band models use the same model parameters as the R-band models, with one exception, $z_{0,i} = 0.95z_{0,R}$, which results in negative slopes in $R-i$ with increasing vertical distance. Thereby, any red-excess haloes in convolved models are induced by the PSF. $\mu_{0,0,R} - \mu_{0,0,i}$ is set to 1.3 mag arcsec^{-2}, which produces a rough agreement with the $V-i$ profile for NGC 5907 of Lequeux et al. (1996, hereafter LFD96)[1]. The used PSF image is twice as large as the model image, to avoid PSF truncation effects in convolved images (see below). The PSF and the model images are resampled to use the same pitch and about 100–200 pixels on the side, typically, to keep calculation times short. All convolutions are made by direct integration.

Convolved surface-brightness profiles are plotted together with model surface-brightness profiles for a cut along the minor axis, directed outwards from the centre on the same (vertical) axis. V- and R-band measurements of NGC 5907 are plotted as well in Sect. 4; I used DEXTER[2] (Demleitner et al. 2001) to extract the data. The three resulting $R-i$ colour profiles are shown in a separate lower panel: the model, the convolved models that used the earlier $\mathrm{PSF}_{V,0\mathrm{m}}$ and $\mathrm{PSF}_{i,0\mathrm{m}}$, and the convolved models that used the later $\mathrm{PSF}_{V,3\mathrm{m}}$ and $\mathrm{PSF}_{i,3\mathrm{m}}$.

The PSF induces scattered light, where surface-brightness profile cuts of input models and convolved models differ. Larger differences between profile cuts of convolved models that use $\mathrm{PSF}_{V,0\mathrm{m}}$, $\mathrm{PSF}_{V,3\mathrm{m}}$, and $\mathrm{PSF}_{\mathrm{K71}}$ in the R band, or $\mathrm{PSF}_{i,0\mathrm{m}}$ and $\mathrm{PSF}_{i,3\mathrm{m}}$ in the i band, are indicators of stronger time dependence in the PSFs. The opposite applies when such differences are smaller. Measured values that are due to scattered light should fall on top of profile cuts of a model that is convolved with the PSF at the time of the observations.

A scattered-light halo radius r_{110} is defined as the smaller limiting radius where the convolved model intensity at all larger radii is ≥ 10 per cent higher than the model intensity. r_{110} depends on both object parameters and the PSF.

[1] The exact difference is unimportant to the demonstration here, where the main point is to illustrate the spatial dependence of the colour profile. All colour profiles are offset by the same value.

[2] DEXTER is available at: http://dexter.sourceforge.net.

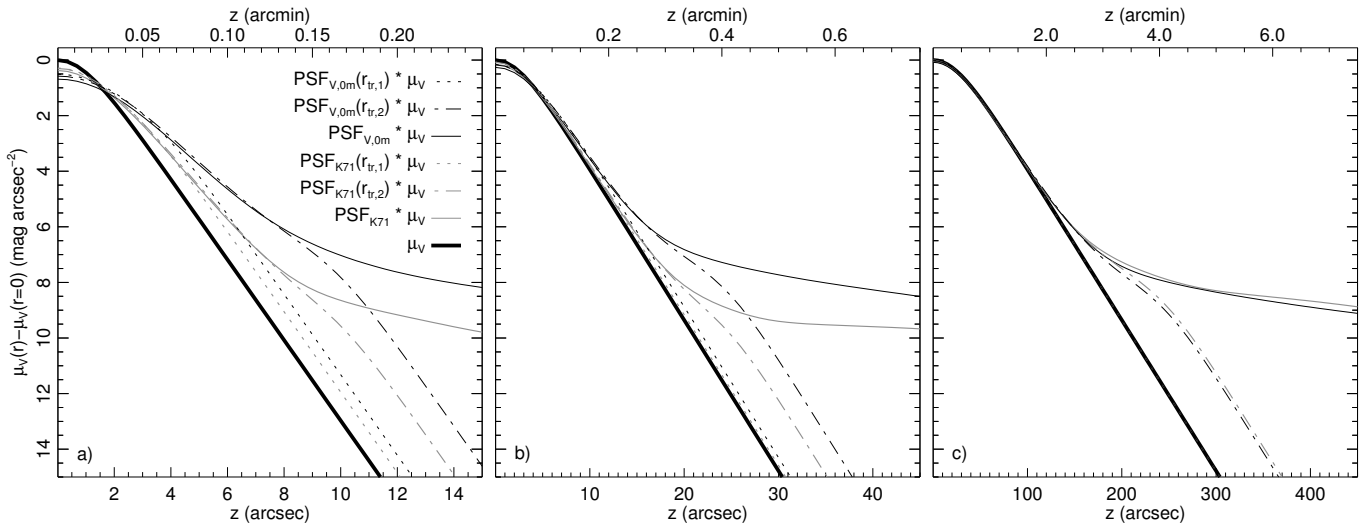

Fig. 5. Vertical-axis surface-brightness profiles that illustrate effects of radial truncation of PSF_{K71} and $PSF_{V,0m}$ in example models. The three panels show: **a**) a small edge-on galaxy, **b**) an edge-on galaxy of intermediate size, and **c**) a large edge-on galaxy. In each panel, the disc-galaxy model profile is drawn with a thick black solid line, and model profiles that were convolved with $PSF_{V,0m}$ (PSF_{K71}) are drawn with thin black (grey) lines. The profile of the model that is convolved with the complete PSF is drawn with a thin solid line. Profiles are also shown where each PSF was truncated at $r_{tr,1}$ ($r_{tr,2}$) with a dotted line (dash-dotted line) in each panel; **a**) $r_{tr,1} = 4''$ and $r_{tr,2} = 10''$; **b**) $r_{tr,1} = 10''$ and $r_{tr,2} = 25''$; **c**) $r_{tr,1} = 10''$ (lines fall on top of the model line and are not visible) and $r_{tr,2} = 250''$ (Table 3).

Table 3. Example model parameters.

	h_r	z_0	$r_{tr,1}$	$r_{tr,2}$
small galaxy	$7\farcs5$	$1\farcs5$	$4\farcs0$	$10''$
medium galaxy	$20''$	$4\farcs0$	$10''$	$25''$
large galaxy	$240''$	$40''$	$10''$	$250''$

Notes. Column 2, major-axis scale length; Col. 3, minor-axis scale height; Col. 4, first truncation radius; and Col. 5, second truncation radius. The parameter $n_s = 1$ in each case.

3.4. Application of the method on three example models

I calculated three example models of a small, an intermediate, and a large galaxy that are viewed edge on, at a high inclination angle, to illustrate consequences of using radially truncated PSFs. I varied the minor-axis scale height z_0 and set $h_r = 5z_0$ and $n_s = 2$. Each model was convolved with PSF_{K71} and an extrapolated $PSF_{V,0m}$. Additionally, each model was convolved with either PSF, after the PSF was truncated at a smaller radius $r_{tr,1}$ or a larger radius $r_{tr,2}$. Model parameters and truncation radii r_{tr} are given for each model in Table 3. The resulting minor-axis surface-brightness profiles are shown in Fig. 5. Values that are quoted in parentheses below used PSF_{K71}, and the other values $PSF_{V,0m}$.

3.4.1. The small galaxy

The convolved profiles show excess scattered light at all distances $z \gtrsim 1\farcs7$ (Fig. 5a), whilst less light is seen at shorter distances (this decrease is largely caused by the seeing-dominated part of the PSFs). The scattered-light halo of the convolved model is too faint for $z \gtrsim 4''$ ($z \gtrsim 4\farcs3$) when the PSF is truncated at $r_{tr} = 4''$. The corresponding value for $r_{tr} = 10''$ is $z \gtrsim 8''$ ($z \gtrsim 8''$). The surface-brightnesses that were calculated using the three versions of the truncated $PSF_{V,0m}$ differ by up to 0.2 mag arcsec^{-2} at the centre, due to the variations of the individual normalization of the PSFs. The correct amount of scattered light at $z = 15''$ is only achieved when the PSF is not truncated within, say, $r \approx 19''$ ($15''\times10''/8''$). Both PSF_{K71} and $PSF_{V,0m}$ are about 10 mag arcsec^{-2} fainter at $r = 15''$, compared to the centre. The model surface brightness is about 8.2 (6.6) mag arcsec^{-2} fainter than the convolved structure at $z = 12''$; the signal-to-noise (S/N) value that would be required to extract the intensity structure of the model structure is about 1900 (440). At $z = 7\farcs5$, the corresponding values are 3.7 mag arcsec^{-2} and S/N≈30 (2.1 mag arcsec^{-2} and S/N≈7).

3.4.2. The intermediate-size galaxy

There is less excess light compared to the small galaxy near the centre, Fig. 5b. The convolved profiles show excess scattered light at all distances $z \gtrsim 5''$, and they overlap each other using either PSF for $z \lesssim 11''$. When the PSF is truncated at $r_{tr} = 10''$, there is an excess due to scattered light of only about 0.5 (0.2) mag arcsec^{-2} for $z \gtrsim 10''$. When the PSF is instead truncated at $r_{tr} = 25''$, the convolved model becomes significantly fainter than the model that is convolved using the full PSF for $z \gtrsim 16''$ ($z \gtrsim 18''$). The correct amount of scattered light at, say, $z = 40''$ is only achieved when PSF is not truncated within, say, $r = 65''$ ($40''\times25''/16''$). Compared to the centre, the PSF is about 12 (14) mag arcsec^{-2} fainter at $r = 40''$. The model surface brightness is about 7.3 (5.6) mag arcsec^{-2} fainter than the convolved structure at $z = 30''$, and the required S/N≈830 (S/N≈170); at $z = 20''$ the corresponding values are about 2.6 mag arcsec^{-2} and S/N≈11 (1.4 mag arcsec^{-2} and S/N≈3.6).

3.4.3. The large galaxy

Using either of the radially complete PSFs, the convolved model shows significant excess that is due to scattered light, beginning at $z \approx 120''$, Fig. 5c. The halo is not reproduced at all when the PSF is truncated at $r_{tr} = 10''$. The scattered-light halo of the convolved model is too faint for $z \gtrsim 160''$ when the PSF is truncated at $r = 250''$. The PSF is about 20 mag arcsec^{-2} fainter at $r = 330''$ than at the centre (see Fig. 1). To measure the modelled intensity at $z \simeq 250''$, which is about 4.1 mag arcsec^{-2} fainter than

the scattered-light halo, the required S/N ≈ 44. The convolved profiles of the two PSFs nearly overlap since they are the same for $r > 200''$. It is important to note that the surface-brightness of the model that is convolved with PSF_{K71} in Fig. 5c is brighter at large radii than in it is in Figs. 5a and 5b; this is expected, because, compared to where $r \lesssim 30''$, the PSF is more shallow at larger radii.

3.4.4. Summarizing the results of the example models

The faintness of the PSF cannot be a limiting factor in accurate analyses of extended edge-on disc galaxies. It is instead the radial extent of the PSF that sets the limit on what can be corrected for. Not only small edge-on galaxies are strongly affected by scattered light, but also large galaxies, and time-dependent variations of the PSF cause variable structures.

The only way to remove scattered light, in the form of galaxy haloes, is through deconvolution with an accurately determined PSF and observations that, at least, cover all brighter regions at high enough signal-to-noise. However, the required accuracy in the measurements quickly becomes enormous with increasing vertical distances, and the required accuracy of the PSF cannot be lower than this, but is likely higher. It should, nevertheless, be safe to use a PSF with a radius that is twice as large as the maximum measured radius, accounting for symmetric objects. The tests above indicate that for these extended edge-on galaxies the minimum radial extent of the PSF is 1.5 times the outermost measured radius of the galaxy.

This study applies to already correctly determined surface-brightness structures and PSFs. Two factors that may play an important role to their determination are the assumed sky background level and scattered light from surrounding objects. Additionally, scattered light also affects the sky background. I show one example of how a slightly different value on the sky background changes the outcome of the analysis for observations of NGC 5907 in Sect. 4.

4. On observations of the edge-on galaxy NGC 5907

An extended faint halo was first found around an edge-on disc galaxy in *R*-band observations of NGC 5907 (Sackett et al. 1994; MBH94). Here, I re-examine the observations in the visual wavelength range of this galaxy with a focus on the role of integrated and time-varying scattered light. My analysis approach is to use both the originally derived PSF_{MBH} and vertical surface-brightness structure of MBH94, as well as PSF^{new}_{MBH} and a surface-brightness structure that I derived myself as a consistency check, using the original data.

4.1. Original observations and the derivation of PSF_{MBH}

The first observations of the halo of NGC 5907 by MBH94 were made using a Harris *R*-band filter with the Kitt Peak National Observatory No. 1 0.9m telescope on 1990 April 29 and 30, as part of a five-night observing run. The two nights were photometric and the seeing was 3.″5. LFD96 made follow-up observations of NGC 5907 using the *V*-band filter with the Canada-France-Hawaii Telescope at a seeing of 1″. The telescope archive reveals that the observations were made on 1995 June 3 to 7. Zheng et al. (1999, hereafter ZSS99) observed NGC 5907 using a BATC 6660Å filter with the Beijing Astronomical Observatory 0.6/0.9m telescope in 23 nights on 1995 January 31 to June 27. The seeing was about 4″. The filter bandwidth ratio of the *R* band (1380Å) to the BATC 6660Å band (480Å) is about 2.9, which corresponds to a magnitude difference of $-1.15\,\mathrm{mag\,arcsec^{-2}}$, assuming a constant intensity across the bandpass. The authors instead apply an offset of $0.3\,\mathrm{mag\,arcsec^{-2}}$ to the *R*-band data of MBH94, to match them with their 6660Å-band data – the chosen value is not further motivated.

MBH94 determine that the error in the 15 sky frames that they use is 1760 ADU (analog-to-digital unit), and the associated error is 5.1–10.3 ADU. They also derive PSF_{MBH}, using two brighter field stars, which extends out to $r = 116''$; this PSF is shown in Fig. 1. Outside the seeing disc, PSF_{MBH} lies above $PSF_{V,0m}$ and $PSF_{V,3m}$ for $r \lesssim 10''$, is closer to $PSF_{V,0m}$ where $20'' \lesssim r \lesssim 70''$, and then turns upwards for larger radii. Additional details on the original observations of NGC 5907 are given in Sect. C.1.

4.2. Reconsidering the analysis of the original data

Two issues with the original study of MBH94 motivate a re-assessed analysis of the measurements: the background in the field around the galaxy does not appear flat on large scales, and the integrated PSF is underestimated when diffraction spikes are masked. I made a detailed reconsideration of the analysis of the originally reduced data of MBH94, cf. Sect. C.2.

A flat background – at the level of a few counts – is important when measuring surface-brightnesses that are only slightly fainter than the sky. The new analysis revealed PSF^{new}_{MBH} that is brighter at larger radii than PSF_{MBH}, see Fig. 1; it is brighter because of a lower background value in the vicinity of the two saturated stars that are used to derive the PSF. The value is only 3–4 ADU lower than the value that MBH94 seem to use, and is within the error bars of their flat-field image (5.1–10.3 ADU). The new PSF^{new}_{MBH} is also mostly within the error bars of PSF_{MBH}. The difference between PSF_{MBH} and PSF^{new}_{MBH} is about $0.5\,\mathrm{mag\,arcsec^{-2}}$ for $40 \lesssim r \lesssim 60''$.

The galaxy image is the result of the convolution with a PSF where diffraction spikes are present, therefore their contribution must not be removed from the PSF when it is used to correct object images for PSF effects. However, the difference due to masked diffraction spikes is small. A masked PSF is, when compared to an unmasked PSF, $0.1\,\mathrm{mag\,arcsec^{-2}}$ fainter at $r \simeq 20''$, this difference decreases to $0.0\,\mathrm{mag\,arcsec^{-2}}$ at $r \simeq 40''$.

4.3. Models of the surface-brightness structure

I modelled NGC 5907 with $h_r = 90''$, $z_0 = 15''$, $n_s = 2$, and assumed $D = 11.7\,\mathrm{Mpc}$. In comparison, MBH94 use the values $h_r = 90''$ and $z_0 = 16''$ (which corresponds to $h_z = z_0/2 = 8.''1$; they specify all parameters in kpc and assume $D = 11\,\mathrm{Mpc}$). Model and observed vertical-axis profiles are shown in Fig. 6a, and corresponding $R - i$ colour profiles in Fig. 6b. The five PSFs that are used in the *R* band cause intensity (colour) differences of up to 1.5 (0.3) $\mathrm{mag\,arcsec^{-2}}$ at $r = 70''$. At the same radius the surface-brightness (colour) profiles of the convolved models are 2.2–3.7 (0.96–1.5) $\mathrm{mag\,arcsec^{-2}}$ brighter than the input model value. The *R*-band (Sackett et al. 1994), 6660Å-band (ZSS99), and *V*-band (LFD96) measurements fall between the convolved profiles of $PSF_{V,0m}$ and $PSF_{V,3m}$ throughout most of the radial range. *V*-band and *R*-band data nearly overlap where $r \lesssim 30''$, and differ by up to about 1 $\mathrm{mag\,arcsec^{-2}}$ at larger radii in the halo.

For $30 \lesssim r \lesssim 95''$, the halo that MBH94 measure is up to about 1 $\mathrm{mag\,arcsec^{-2}}$ brighter than the model that was convolved with PSF_{MBH}. According to the authors, the halo is not scattered light. However, the conclusion is different with PSF_{MBH} using

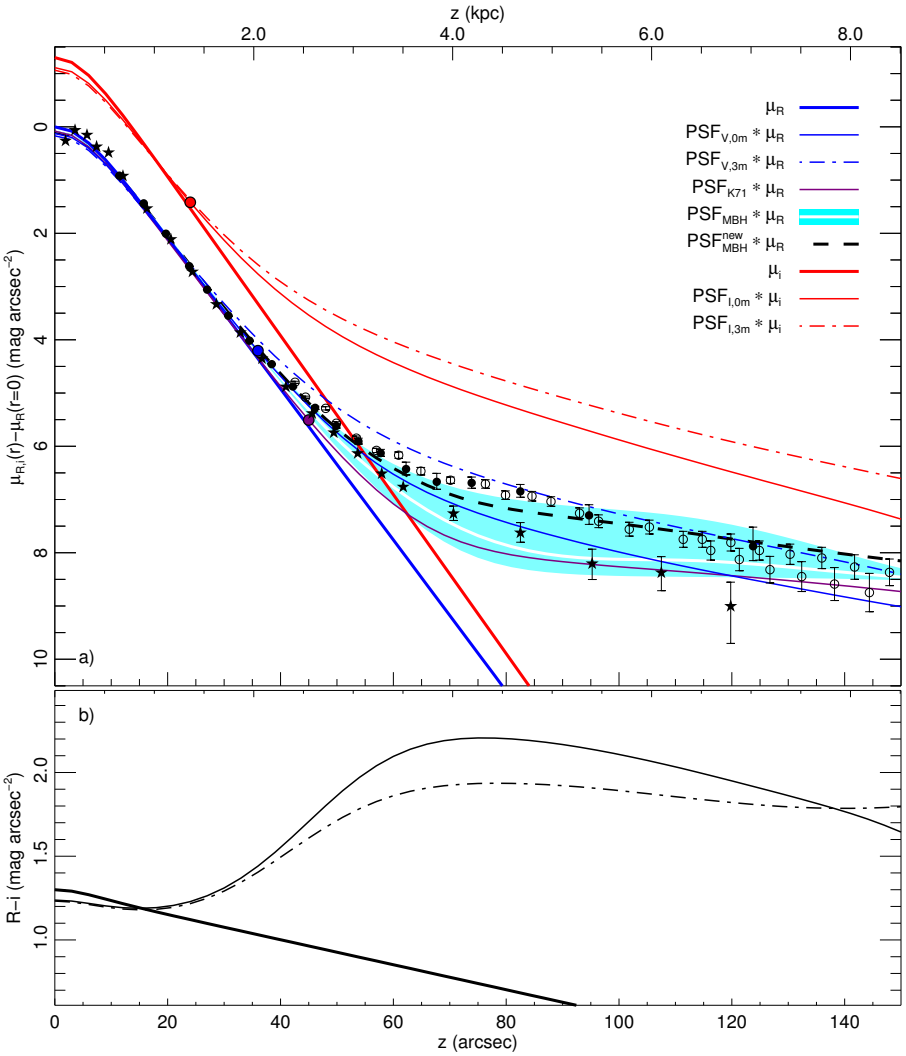

Fig. 6. Vertical-axis R-band and i-band surface-brightness profiles versus the vertical distance z of models and measurements of the edge-on galaxy NGC 5907. **a**) Blue and purple lines show R-band profiles, and red lines i-band profiles. Model profiles are drawn with thick solid lines. Solid (dash dotted) lines are profiles of convolved models using $\mathrm{PSF}_{V,0\mathrm{m}}$ and $\mathrm{PSF}_{i,0\mathrm{m}}$ ($\mathrm{PSF}_{V,3\mathrm{m}}$ and $\mathrm{PSF}_{i,3\mathrm{m}}$), the purple line used $\mathrm{PSF}_{\mathrm{K71}}$. Three different symbols and error bars show measured values: • R band (Sackett et al. 1994; MBH94), ⋆ V band (LFD96), and from profiles on both sides of the disc ∘ 6660Å band (ZSS99). The R-band model was convolved with the measured $\mathrm{PSF}_{\mathrm{MBH}}$ (including lower and upper errors) to produce the white line (cyan-coloured region). The lower limiting radius r_{110} – where the convolved models using $\mathrm{PSF}_{V,0\mathrm{m}}$, $\mathrm{PSF}_{i,0\mathrm{m}}$, and $\mathrm{PSF}_{\mathrm{K71}}$ lie ≥ 10 per cent above the input model – is marked with a coloured bullet with a black border. **b**) Three colour profiles $R-i$ are shown for: the model (thick solid line), the convolved model using $\mathrm{PSF}_{V,0\mathrm{m}}$ and $\mathrm{PSF}_{i,0\mathrm{m}}$ (solid line), and the convolved model using $\mathrm{PSF}_{V,3\mathrm{m}}$ and $\mathrm{PSF}_{i,3\mathrm{m}}$ (dash-dotted line).

its upper error bars, and with $\mathrm{PSF}^{\mathrm{new}}_{\mathrm{MBH}}$, which convolved models nearly overlap all measured values, but the two ones at $r = 74''$ and $r = 83''$. The upturn in the outer part of $\mathrm{PSF}_{\mathrm{MBH}}$ and $\mathrm{PSF}^{\mathrm{new}}_{\mathrm{MBH}}$ causes a shelf of nearly constant brightness in the convolved model profile where $80 \lesssim r \lesssim 115''$ – there is no corresponding shelf in the measurements[3]. Considering the difficulties in measuring $\mathrm{PSF}^{\mathrm{new}}_{\mathrm{MBH}}$ accurately at both smaller and larger radii (Sect. C.2), it cannot be excluded that all of the measurements can be explained as scattered light. $\mathrm{PSF}^{\mathrm{new}}_{\mathrm{MBH}}$ is particularly noisy in the range $70 \lesssim r \lesssim 95''$, which delimits the accuracy of two values that are brighter than the convolved model. Under the assumption that the measurements are scattered light, at $z = 70''$ the required S/N of the measurements to measure the 2.5 mag arcsec^{-2} fainter input model is 10. The accuracy requirement quickly grows to enormous values at larger distances, where it is impossible to measure the exponential structure (also see Sect. 3.4).

According to ZSS99, the 0.3 mag arcsec^{-2} offset, which they adopt between the R-band and the 6660Å-band measurements, occurs due to different filter bandwidths. Under the assumption that the halo is scattered light, varying PSFs justify deviating measurements, also the 1 mag arcsec^{-2} fainter V-band measurements of LFD96. I have no J-band or K-band PSFs to model the near-infrared observations of Rudy et al. (1997) or James & Casali (1998), but the PSFs of these bands – as measured with, for example, data of the 2MASS Large Galaxies Atlas (Jarrett et al. 2003, where observations were made at Mt. Hopkins in Arizona and the Cerro Tololo Inter-American Observatory) – are even brighter at larger radii than the I-band PSF (Michard 2007), and scattered-light effects are therefore even stronger.

The $R-i$ colour profiles of the convolved models in Fig. 6b show red excess where $z > 18''$, in qualitative agreement with the $V-I$ profile of LFD96 (see their fig. 3). The difference between the colour profiles that were derived using $\mathrm{PSF}_{V,0\mathrm{m}}$ and $\mathrm{PSF}_{i,0\mathrm{m}}$, versus $\mathrm{PSF}_{V,3\mathrm{m}}$ and $\mathrm{PSF}_{i,3\mathrm{m}}$, illustrate that derived colours in the halo, which is dominated by scattered light, completely depend on the PSFs in the used bandpasses. Whilst $\mathrm{PSF}_{V,0\mathrm{m}}$ and $\mathrm{PSF}_{i,0\mathrm{m}}$ contain fainter wings than $\mathrm{PSF}_{V,3\mathrm{m}}$ and $\mathrm{PSF}_{i,3\mathrm{m}}$, their radial difference is greater, which result in more red excess in the halo.

5. Discussion and conclusions

I have presented a first detailed overview and comparison of already measured radially extended PSFs, since the first summary of K71 and the more recent summary of B07. The overview demonstrates that all PSFs are expected to continue to large radii (angles), and that our knowledge is poor of how the PSF varies with the time and the wavelength, in particular at large radii. de Vaucouleurs (1958) and later K71 (amongst a few others), find

[3] It was necessary to extrapolate $\mathrm{PSF}_{\mathrm{MBH}}$ and $\mathrm{PSF}^{\mathrm{new}}_{\mathrm{MBH}}$ with a decreasing slope outside their largest radii to avoid positive slopes in the outer regions of convolved model profiles.

that the PSF declines as an r^{-2} power-law at large distances. B07 presents a summary of PSFs to show that various measurements contradict the use of a general r^{-2} slope. I have normalized all PSFs and put them in the same plot, and the result shows no evidence against an r^{-2} power-law slope at large radii. Instead, several radially extended measurements point at a more shallow decline. There is one exception, the PSF of Abraham & van Dokkum (2014), which is measured with the only configuration that uses refractive instead of reflective optics. Encircled energy plots show significant amounts of light in the far wings of the PSF, and there is currently no clear correspondence between the amount of encircled energy in the outer parts of the PSF and atmospheric extinction.

Early studies measured the outer parts of the PSF with observations of planets, the Moon, and the Sun, instead of using (only) stars. I have shown that extended objects can be regarded as point sources, beginning at a geometry-dependent radius. Complementary observations of these comparatively bright objects will make possible more accurate measurements of varying and radially extended PSFs. An additional point of concern that I have not addressed here, is how the PSF changes across the surface, away from the optical axis (SHM09); new PSF measurements need to take such issues into account as well.

I have studied the role of scattered light to shape the surface-brightness structure of three models of edge-on disc galaxies; the model set consisted of a small galaxy, an intermediate-sized galaxy, and a large galaxy, which all contain a single thin disc. I have used $\mathrm{PSF_{K71}}$ (K71) as a lower limit, and $\mathrm{PSF_{}}_{V,0\mathrm{m}}$ (Michard 2002) as a slightly-above average indicator of scattered-light effects. The results show that in the case of edge-on galaxies it is necessary to use a PSF that extends to at least 1.5 times the measured radius, regardless of the size of the galaxy, or the measurements cannot be corrected; it seems that it would be safe, for any measurement, to use a PSF of twice the measured radius. It is notable that the requirements on the accuracy of the measurements at large vertical distances quickly becomes insurmountable to measure an underlying exponential component.

Surface-brightness profiles of edge-on galaxies are divided into four components: a centre bulge, a thin disc, a thick disc, and a halo. The first faint diffuse halo around an edge-on disc galaxy was found around the Sc-type NGC 5907. Examples of explanations to the origin of the halo include that it traces the dark-matter halo (Sackett et al. 1994), and that parts or all matter in the halo could be low-mass stars (Sackett et al. 1994; LFD96). Zepf et al. (2000) find one halo star in their *HST* H-band observations of NGC 5907, instead of the expected 100; they favour a stellar population with a very high dwarf-to-giant ratio to explain the halo. Yost et al. (2000) present near-infrared observations from above the Earth atmosphere, and rule out hydrogen-burning stars as a possible cause of the halo. Shang et al. (1998), ZSS99, and Martínez-Delgado et al. (2008) discover and discuss comparatively faint stellar tidal streams that extend far out from NGC 5907 on its north-east and south-west sides. The influence of the tidal streams on the results presented here is minor, despite that the streams partly overlap the regions that are used to measure the galaxy profile and the PSFs; the reason is that the relative intensity between the streams and the background is very small, and even smaller than the errors in the reduced image of MBH94. ZSS99 also find that vertical surface-brightness structures away from the minor axis are asymmetric, and conclude that the halo is not real, but is contaminated by light from the stream and residual light from field stars. They do not consider scattered light from the galaxy itself.

Scattered light was dismissed as an explanation to the halo by MBH94 after a careful analysis of the PSF, which later studies of this galaxy do not address with as much care. I have reassessed the original analysis of NGC 5907, regarding the role of scattered light, and I have come to the conclusion that it likely is the major reason to the appearance of the halo. Specifically, I have analysed the influence of the variations in the galaxy background. I have lowered the background value by 3 ADU (0.17%), compared to the value that was seemingly used to measure the extended original $\mathrm{PSF_{MBH}}$. I have then measured a significantly brighter $\mathrm{PSF^{new}_{MBH}}$, where the new PSF is still mostly within the error bars of $\mathrm{PSF_{MBH}}$. MBH94 quote the accuracy of their sky data as 10.3 ADU, which is more than three times as large as the background offset that I applied. The new finding illustrates the high accuracy that is required of both the PSF and the measurements when dealing with scattered light.

Finally, the $R - i$ colour profiles of the scattered-light dominated halo of the models show very strong red excess, which is all caused by the shape of the PSFs. Notably, J08 comes to the same conclusion, based on models that are convolved with less extended PSFs. It seems that the CCD-specific red-halo effect (Sirianni et al. 1998) plays a strong role to enhance the red excess in the i-band.

I emphasize that the object asymmetry and the varying background complicate the modelling. Measurements of other authors of NGC 5907 agree with this conclusion. In particular, it appears that the observations of LFD96 were made with a fainter V-band PSF that is similar to $\mathrm{PSF_{K71}}$, whilst $\mathrm{PSF^{new}_{MBH}}$ is brighter than $\mathrm{PSF_{}}_{V,0\mathrm{m}}$ throughout most of the radial range. Assuming that the halo is induced by the PSF, there is also no argument against a larger offset value between the R and the 6660Å bandpasses that ZSS99 use. In view of the alternative explanations to the bright measurements in the halo of NGC 5907, the one of scattered light is simple, and does not require any exotic stellar populations. Despite very small adjustments to values that were used in the analysis, the impact on physical results is large.

With his study on two sets of smaller edge-on galaxies, J08 points out that effects of scattered light in observations of edge-on disc galaxies can be significant. The conclusion of this paper is that these effects can be even stronger – faint regions around edge-on galaxies of all sizes are affected by scattered light. I have indicated that PSFs generally vary with time and wavelength, and that also their faint outer wings contribute significantly to observed structures. The question is, in view of this new awareness, how observations of astronomical objects and their faint structures in general are affected by scattered light? In a second paper, I will study the influence of scattered light on a larger set of models and observations of different types of galaxies.

Acknowledgements. I am most grateful to H. Morrison, who provided me with the originally reduced images of NGC 5907. I thank R. Abraham for sending me the Dragonfly Array PSF data. I thank A. Partl, A. Monreal-Ibero, R. de Jong, C. Vocks, and M. M. Roth for comments on the manuscript. This research was supported by funds of PTDESY-05A12BA1.

References

Abraham, R. G. & van Dokkum, P. 2014, ArXiv e-prints
Beckwith, S. V. W., Stiavelli, M., Koekemoer, A. M., et al. 2006, AJ, 132, 1729
Bergvall, N., Zackrisson, E., & Caldwell, B. 2010, MNRAS, 405, 2697
Bernat, A. P. & Lambert, D. L. 1975, ApJ, 201, L153
Bernstein, R. A. 2007, ApJ, 666, 663 (B07)
Brown, G. S. 1978, in Modern Techniques in Astronomical Photography, ed. R. M. West & J. L. Heudier (Geneva: ESO), 169–174
Capaccioli, M. & de Vaucouleurs, G. 1983, ApJS, 52, 465 (CV83)

Corradi, R. L. M., Schönberner, D., Steffen, M., & Perinotto, M. 2003, MNRAS, 340, 417
de Jong, R. S. 2008, MNRAS, 388, 1521 (J08)
de Vaucouleurs, G. 1948, Annales d'Astrophysique, 11, 247
de Vaucouleurs, G. 1953, MNRAS, 113, 134
de Vaucouleurs, G. 1958, ApJ, 128, 465
de Vaucouleurs, G. & Capaccioli, M. 1979, ApJS, 40, 699
Deirmendjian, D. 1957, Annales de Geophysique, 13, 286
Deirmendjian, D. 1959, Annales de Geophysique, 15, 218
Demleitner, M., Accomazzi, A., Eichhorn, G., et al. 2001, in ASP Conf. Ser., Vol. 238, ADASS X, ed. F. R. Harnden, Jr., F. A. Primini, & H. E. Payne (San Francisco: ASP), 321–324
Feldmeier, J., Hagen, A., Ciardullo, R., et al. 2013, ApJ, 776, 75
Gonzalez, A. H., Zabludoff, A. I., & Zaritsky, D. 2005, ApJ, 618, 195
González Delgado, D., Olofsson, H., Schwarz, H. E., Eriksson, K., & Gustafsson, B. 2001, A&A, 372, 885
Gustafsson, B., Eriksson, K., Kiselman, D., Olander, N., & Olofsson, H. 1997, A&A, 318, 535
Hasan, H. & Burrows, C. J. 1995, PASP, 107, 289
Idiart, T. P., Michard, R., & de Freitas Pacheco, J. A. 2002, A&A, 383, 30
James, P. A. & Casali, M. M. 1998, MNRAS, 301, 280
Jarrett, T. H., Chester, T., Cutri, R., Schneider, S. E., & Huchra, J. P. 2003, AJ, 125, 525
King, I. R. 1971, PASP, 83, 199 (K71)
Kormendy, J. 1973, AJ, 78, 255
Krisciunas, K. & Schaefer, B. E. 1991, PASP, 103, 1033
Krist, J. & Burrows, C. 1992, Large Angle Scattering in WFPC2 and Horizontal "Smearing" Correction, Tech. rep., Space Telescope Science Institute
Krist, J. E. 1995, in Calibrating Hubble Space Telescope. Post Servicing Mission, ed. A. P. Koratkar & C. Leitherer (Baltimore: Space Telescope Science Institute), 311–321
Krist, J. E., Hook, R. N., & Stoehr, F. 2011, in Proc. SPIE, Vol. 8127, Optical Modeling and Performance Predictions V., ed. M. A. Kahan (Bellingham: SPIE)
Lequeux, J., Fort, B., Dantel-Fort, M., Cuillandre, J.-C., & Mellier, Y. 1996, A&A, 312, L1 (LFD96)
Mackie, G. 1992, ApJ, 400, 65
Martínez-Delgado, D., Peñarrubia, J., Gabany, R. J., et al. 2008, ApJ, 689, 184
Mauron, N. & Caux, E. 1992, A&A, 265, 711
Michard, R. 1953, Annales d'Astrophysique, 16, 217
Michard, R. 2002, A&A, 384, 763
Michard, R. 2007, A&A, 464, 507
Middlemass, D., Clegg, R. E. S., & Walsh, J. R. 1989, MNRAS, 239, 1
Monreal-Ibero, A., Roth, M. M., Schönberner, D., Steffen, M., & Böhm, P. 2006, New A Rev., 50, 426
Morrison, H. L., Boroson, T. A., & Harding, P. 1994, AJ, 108, 1191 (MBH94)
Örndahl, E., Rönnback, J., & van Groningen, E. 2003, A&A, 404, 883
Patat, F. 2003, A&A, 400, 1183
Piccirillo, J. 1973, PASP, 85, 278
Pierce, A. K. 1954, ApJ, 120, 221
Plez, B. & Lambert, D. L. 1994, ApJ, 425, L101
Racine, R. 1996, PASP, 108, 699
Redman, R. O. & Shirley, E. G. 1938, MNRAS, 98, 613
Rönnback, J., van Groningen, E., Wanders, I., & Örndahl, E. 1996, MNRAS, 283, 282
Rudy, R. J., Woodward, C. E., Hodge, T., Fairfield, S. W., & Harker, D. E. 1997, Nature, 387, 159
Sackett, P. D., Morrison, H. L., Harding, P., & Boroson, T. A. 1994, Nature, 370, 441
Sandin, C., Schönberner, D., Roth, M. M., et al. 2008, A&A, 486, 545
Shang, Z., Zheng, Z., Brinks, E., et al. 1998, ApJ, 504, L23
Shectman, S. A. 1974, ApJ, 188, 233
Sirianni, M., Clampin, M., Hartig, G. F., et al. 1998, in Proc. SPIE, Vol. 3355, Optical Astronomical Instrumentation, ed. S. D'Odorico (Bellingham: SPIE), 608–612
Sirianni, M., Jee, M. J., Benítez, N., et al. 2005, PASP, 117, 1049
Slater, C. T., Harding, P., & Mihos, J. C. 2009, PASP, 121, 1267 (SHM09)
Surma, P., Seifert, W., & Bender, R. 1990, A&A, 238, 67
Tal, T. & van Dokkum, P. G. 2011, ApJ, 731, 89
Tziamtzis, A., Schirmer, M., Lundqvist, P., & Sollerman, J. 2009, A&A, 497, 167
Uson, J. M., Boughn, S. P., & Kuhn, J. R. 1991, ApJ, 369, 46
van de Hulst, H. C. 1948, in The Atmospheres of the Earth and Planets, ed. G. P. Kuiper (The University of Chicago Press, Chicago), 49–111
van der Kruit, P. C. 1988, A&A, 192, 117
van der Kruit, P. C. & Searle, L. 1981, A&A, 95, 105
Wisotzki, L., Schechter, P. L., Bradt, H. V., Heinmüller, J., & Reimers, D. 2002, A&A, 395, 17
Wu, H., Burstein, D., Deng, Z., et al. 2002, AJ, 123, 1364
Yost, S. A., Bock, J. J., Kawada, M., et al. 2000, ApJ, 535, 644
Zepf, S. E., Liu, M. C., Marleau, F. R., Sackett, P. D., & Graham, J. R. 2000, AJ, 119, 1701
Zheng, Z., Shang, Z., Su, H., et al. 1999, AJ, 117, 2757 (ZSS99)
Zibetti, S., White, S. D. M., & Brinkmann, J. 2004, MNRAS, 347, 556

Appendix A: About *HST* PSFs

PSFs that are measured with the *HST* – and other space-based telescopes – are less affected by dust and the Earth atmosphere than PSFs of ground-based telescopes, and they are often much more compact. The tool Tiny Tim (Krist et al. 2011) was created to provide model PSFs for all instruments and most observing modes of the *HST*. The tool, its documentation, and additional information are available at the project web site[4]. Tiny Tim makes a best effort to account for all factors in the optical path that affect the PSF (see the Tiny Tim user guide). The resulting PSFs are many times of good quality, considering that many of these factors vary with time or field position. One comment below the 'Performance' section at the project web site is relevant to this study:

> For PSF subtraction where details of the outer portions of the distribution are important, and for other cases where accurate PSF characterizations are needed, these modelled PSFs may lack suitable accuracy, and empirical PSF techniques should be considered when practical.

This is a highly important comment, considering that in this paper I demonstrate the decisive influence of the outer faint regions of the PSF to induce haloes and affect colour profiles.

I mention additional content of two sections in the Tiny Tim user guide (version 6.3) that are related to this issue. Light is scattered into the outer regions of the PSF of the second Wide Field and Planetary Camera (WFPC2; Krist & Burrows 1992; Krist 1995); outer regions of the PSF will be underestimated since this effect is not included in Tiny Tim. Furthermore, due to a defect in the high-resolution CCD (HRC) of the Advanced Camera for Surveys (ACS), a halo is created that surrounds the PSF for wavelengths $\lambda > 600$nm; Tiny Tim provides a first estimate of the halo effect. In the ACS instrument handbook[5], the halo is said to appear for $\lambda > 700$nm (HRC) and $\lambda > 900$nm [wide field camera (WFC)].

Sirianni et al. (2005) present measurements of the ACS PSFs where they consider $r = 5\farcs5$ a safe extent to measure all flux within an 'infinite' aperture; they treat all filters of both the HRC and the WFC. I show in Sect. 3.4 how important it is to use a PSF that is not truncated or underestimated at large radii, and I advocate the use of a PSF that is at least 1.5 times as extended as the vertical distance of the edge-on galaxy. It would be valuable to see how an extension of the PSF to, say, $r = 10''$ would affect integrated scattered light in a study that is similar to what I present here for ground-based telescopes – this would show if radially extended PSFs make any difference also with *HST* data.

Appendix B: Details of the extrapolation and normalization of the discussed PSFs

I extrapolated $\mathrm{PSF_{K71}}$, $\mathrm{PSF_{\mathit{V},0m}}$, and $\mathrm{PSF_{\mathit{V},3m}}$ to $r = 90°$, assuming a power law dependence r^{-2}; in agreement with the existing outer parts of $\mathrm{PSF_{K71}}$, $\mathrm{PSF_{P73}}$(▲), and $\mathrm{PSF_{S09}}$. Studies that report on contradicting slopes present a noisy outer PSF that does not extend very far ($\mathrm{PSF_{B07}}$, SDSS PSFs).

The spectroscopic $\mathrm{PSF_{P,LR}}$ (seeing $0\farcs8$) does not extend far; it was extrapolated with $\mathrm{PSF_{CV}}$, as the two PSFs match well in the range $4 \leq r \leq 25''$. I could shift three PSFs precisely, with available information on how they overlap other PSFs: $\mathrm{PSF_{K73}}$,

[4] The Tiny Tim web site at the STScI: http://tinytim.stsci.edu.
[5] The ACS instrument handbook is available at: http://www.stsci.edu/hst/acs/documents/handbooks/current/cover.html.

PSF_{P73} (which triangle-symbol points overlap the aureole line of PSF_{K71}), and $PSF_{V,0m}$. $PSF_{V,3m}$, $PSF_{i,0m}$, and $PSF_{i,3m}$ are fixed relative to $PSF_{V,0m}$. PSF_{S09} is not measured at small radii, which is why I offset it by +0.25 mag arcsec^{-2}, to match it with the other PSFs, the true value could be slightly lower or higher. Abraham & van Dokkum (2014) fix the offset between PSF_{A14} and PSF_{S09}, I used the same value. I offset the SDSS PSFs by hand, to have them agree with the integrated PSFs. These PSFs are poorly determined near their outer limit at $r \simeq 30$–$60''$, which makes an accurate extrapolation to larger radii difficult. PSF_{MBH} is also poorly determined at large radii; I offset it by -13.6 mag arcsec^{-2} to have this large-seeing PSF slightly fainter at the centre than $PSF_{V,0m}$. I used the same offset with PSF^{new}_{MBH}.

The measurements of PSF_{S74} and PSF_{M92} were offset by -7 mag arcsec^{-2} to overlap PSF_{K71}, and all three versions of PSF_{G05} were offset by -12 mag arcsec^{-2} to overlap $PSF_{i,0m}$. These three PSFs were not measured in the centre, and the true offsets could be both slightly larger and slightly smaller. Finally, the (centred) PSF_{B07} was offset to agree with PSF_{K71} in the centre region.

Appendix C: Details of the analysis of NGC 5907

This section contains supplementary details to the discussion of the original analysis and the reconsidered analysis of NGC 5907 in Sect. 4.

Appendix C.1: Details of the original observations

To make possible a careful flat fielding of their data, MBH94 took 22 1800 s exposures of the sky during the five nights of the observing run; these sky regions were offset some 1° from the galaxies of their study. Out of the 22 frames they use 15 frames that are judged to be free from bright stars or defects that could compromise the flat field. The sky frames have about 1760 ADU per pixel, which ought to produce a flatfield where pixel-to-pixel errors are smaller than about 0.29 per cent (5.1 ADU). They make a more detailed error model of the sky, and derive an error of the rotated and shifted sky-image pixels as 0.60 per cent (10.5 ADU), which agrees well with their empirically measured value 0.59 per cent (10.3 ADU).

MBH94 use several bright, but not saturated, stars, to measure the inner parts of a PSF. They measure the outer PSF with the two bright and saturated stars that are seen to the lower left of the galaxy disc in their fig. 1; their figure is reproduced here in Fig. C.1. To this end they prepare and apply a mask that removes all stars, diffraction spikes, and background galaxies in the field around each star. The unmasked pixels are averaged in radial annuli around the centre, starting at $r = 20$ px. The resulting PSF_{MBH} is reproduced in Fig. 1 (and also with its error bars in Fig. C.2), it extends out to $r = 116''$.

Later, LFD96 claim to measure a PSF that reaches 10^{-7} of the peak intensity at $r = 16''$ (the PSF is not published). This PSF is likely incorrectly measured, as it is (along with the SDSS PSFs of Zibetti et al. 2004) much steeper than any of the other PSFs in Figs. 1 and 2. ZSS99 also claim to derive a PSF, but there is no information about how far radially and deeply it extends.

The vertical surface-brightness structure of NGC 5907 is measured after dust and stars are masked, and remaining pixels are averaged in 100 pixel wide strips, which heights change exponentially from 5 px near the major axis to a maximum of 99 px at the vertical distance $z = 160''$. The mask they use is shown in fig. 3 in MBH94.

Table C.1. Image statistics of selected background regions in Fig. C.1.

Id	x	y	min(z)	max(z)	$\bar{z}$	med(z)	σ_z	T
a	143	232	1737.0	1783.3	1759.1	1759.3	7.1	x
b	154	116	1728.8	1778.5	1753.5	1753.2	6.5	x
c	320	545	1737.2	1787.5	1760.4	1760.4	7.0	○
d	352	268	1732.1	1806.9	1759.7	1759.3	7.8	●
e	275	140	1736.7	1777.1	1757.9	1757.9	6.8	x
f	730	490	1736.8	1783.2	1761.8	1761.9	6.9	-
g	1005	1063	1734.3	1785.7	1759.5	1759.4	6.7	-
h	353	899	1733.8	1780.0	1758.5	1758.6	6.7	○
i	701	895	1739.6	1783.3	1759.9	1759.8	6.5	○
j	1078	291	1734.7	1790.6	1762.3	1762.1	7.0	-
k	1201	451	1739.8	1790.6	1764.2	1764.1	6.9	-
l	151	951	1732.2	1782.4	1757.6	1757.6	6.7	-

Notes. Column 1, identifier; Cols. 2 and 3, x- and y-positions of ring centre (px.); Cols. 4–8, minimum, maximum, mean, median, and standard-deviation values (ADU) of, in each case, 1257 pixels z_i inside a ring with the radius 20 px that is centred on the coordinates (x, y); and Col. 9, four symbols specify if the region falls on top of the (T)idal streams around NGC 5907 that are seen in fig. 2 in Martínez-Delgado et al. (2008): x outside of the field, - away, ○ partly on top, ● right on top.

Table C.2. Bright stars in Fig. C.1 that were used to derive a PSF.

Id	x	y	bg.	r_{max}	colour	T
1	195	409	1759	115.5	black solid	○
2	262	252	1759	115.5	black dash dotted	○
3	801	870	1762	13	blue	○
4	840	193	1760	25	magenta	-
5	256	565	1758	24	red	●
6	1164	1126	1760	20	orange	x
7	395	894	1758	18	purple	●

Notes. Column 1, identifier; Cols. 2 and 3, x- and y-positions in the reduced image (px.); Col. 4, used background value (ADU); Cols. 5 and 6, maximum radius (arcsec) and line colour in Fig. C.2; and Col. 7, four symbols specify if the region falls on top of the (T)idal streams around NGC 5907 that are seen in fig. 2 in Martínez-Delgado et al. (2008): x outside of the field, - away, ○ partly on top, ● right on top.

Appendix C.2: Details of the reconsidered analysis

Following the approach of MBH94, I derived a PSF by averaging unmasked pixels in radial annuli around the centre of bright stars. Whilst MBH94 quote a background value of 1760 ADU in the sky image, that value does not seem to apply in all parts of the galaxy image. To quantify the differences I measured background values in different regions in Fig. C.1; image statistics of twelve regions *a*–*l* are shown in Table C.1. In the same table I also marked whether the respective region falls on top of the tidal streams around NGC 5907, as are visible in Martínez-Delgado et al. (2008).

This test shows slightly lower values on the left-hand side of the image, and near the two saturated stars. As a compromise, I estimated that the average background of the regions *a*, *d*, and *e* near the lower saturated star (2) is 1759 ADU. This value is a bit uncertain, and it is possible that it varies by, say, about 2 ADU in the radial range away from each saturated star. The same values also illustrate the difficulties in measuring a PSF at the level of the background with these data, in particular for radii $r \gtrsim 100$ px where all three background regions fall inside the measured region; here, scattered light from star 2 makes these

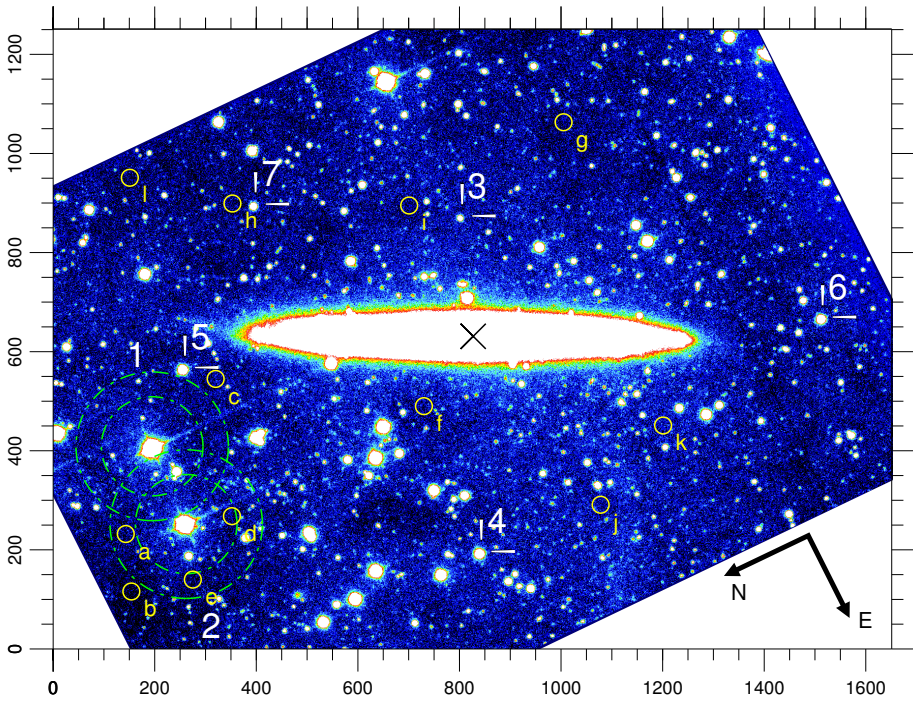

Fig. C.1. The originally reduced image of MBH94 for NGC 5907, shown with a colour map that emphasizes the variations of the background field (their fig. 1b). The unit of the axes is pixels. The used galaxy centre position is marked with an ×. Two sets of green circles indicate the distance at 100 and 150 px away from the two saturated stars 1 and 2. The positions of five bright stars (twelve regions that were used to measure the background) are indicated with markers and a number (circles and a character), cf. Table C.2 (Table C.1).

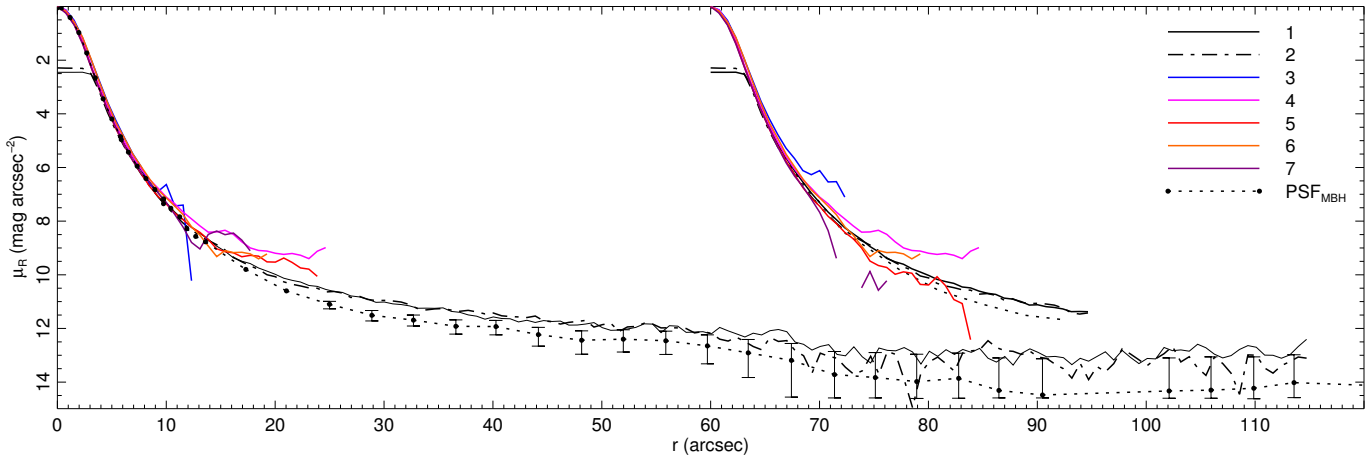

Fig. C.2. PSFs that were derived from the reduced *R*-band image of NGC 5907 (Fig. C.1). The azimuthal average is drawn as magnitude versus radius. The left-hand set of lines used individually set background values. The set of lines that are offset by 60″ were all derived using the background value 1760 ADU. $\mathrm{PSF_{MBH}}$ is drawn with a dotted line, together with its error bars. The saturated-star PSFs are drawn with black solid (1) and dash dotted (2) lines – $\mathrm{PSF^{new}_{MBH}}$ is the average of these two PSFs. The PSF of the remaining five bright stars are drawn with coloured lines out to a maximum radius r_{max}, cf. the legend and Table C.2.

values higher than the sky background. The two stars are also situated right next to a tidal stream around NGC 5907 (compare the position of region *d* with fig. 2 in Martínez-Delgado et al. 2008), but this is not obvious when comparing the values of the separate regions.

The background is brighter on the right-hand side of the image, where I measured 1759.5–1764.2 ADU in the regions *g*, *i*, *j*, and *k*. None of these regions falls directly on top of a tidal stream. For comparison, in the other parts of the galaxy, MBH94 measure a lower value in the region that is offset by 100 px (4.1 kpc) to the left of the galaxy centre, which they attribute a flat-fielding defect. In this region, *f*, I measured the mean value 1761.8 ADU, which is slightly lower than in the regions *j* and *k*, but still significantly higher than the mean value 1759 ADU around the lower saturated star 2. All background values that are quoted here fall within the statistical accuracy of 5–10 ADU.

I derived a PSF for five bright stars in Fig. C.1, using both 1760 ADU and an individually selected value as background, cf. Table C.2; the PSF of each of these relatively faint stars is only useful out to an approximative radius that I refer to as r_{max}. I also derived more extended PSFs for the same saturated stars as MBH94. The brighter contour levels and the regions that I masked around these two stars are shown in Fig. C.3. The original $\mathrm{PSF_{MBH}}$ is shown together with the new PSFs of all seven stars in Fig. C.2.

PSFs that are measured in different parts of the image should overlap (neglecting spatial differences across the field such as reported by SHM09, and which magnitudes are in any case unknown here). The PSFs of stars 1 and 2 are slightly closer to $\mathrm{PSF_{MBH}}$ when the background value 1760 ADU is used, and they nearly overlap when the value is instead 1762 ADU (not shown). The PSF of star 3, which is located above the galaxy

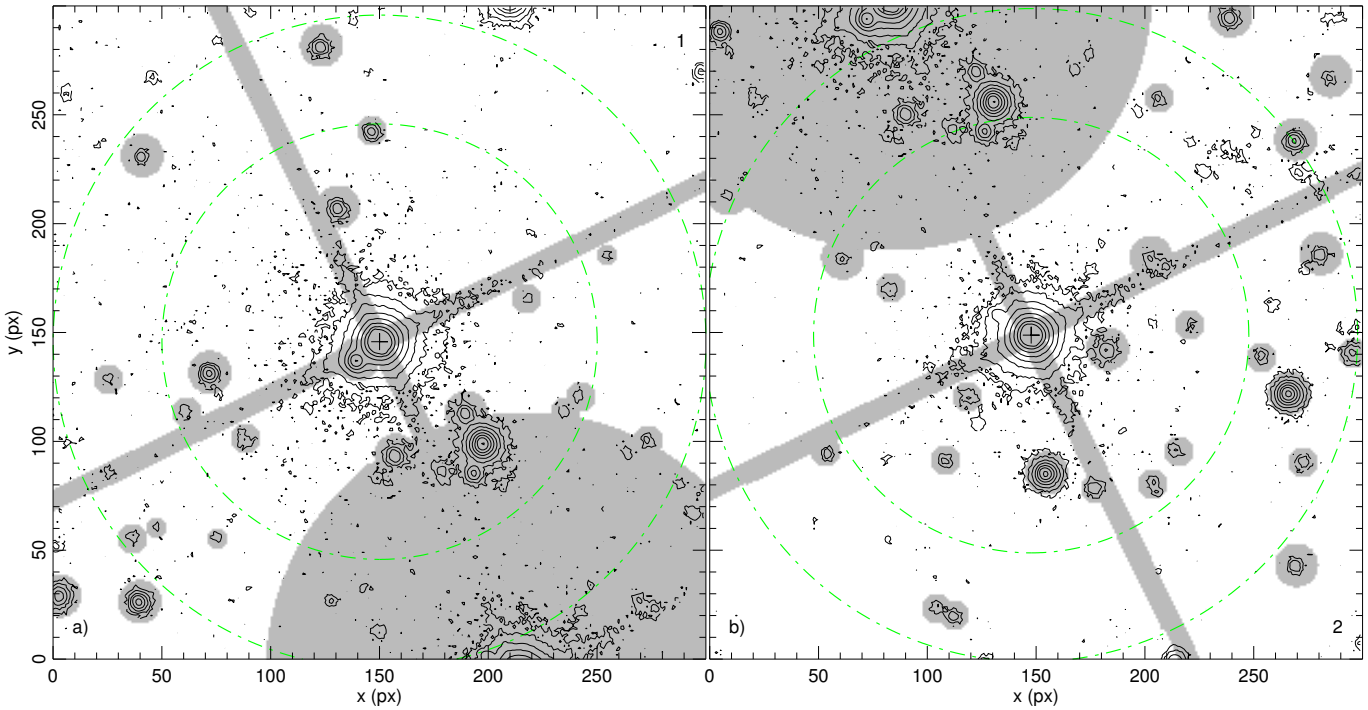

Fig. C.3. Contour plots of the two saturated stars **a**) 1 and **b**) 2 in Fig. C.1, where masked regions are marked in grey. The grey tilted crosses indicate the masked diffraction spikes. The green circles mark the radii 100 and 150 px.

disc in Fig. C.1, lies above the other PSFs in the region $r \gtrsim 5''$. It overlaps the other PSFs better when the background is set to 1762 ADU, which seems to be an appropriate background value in the neighbourhood of this star. The stars 4 and 6 are located right and below of the galaxy disc; their PSFs seem to overlap the other PSFs using the background value 1760 ADU. The stars 5 and 7 are located to the left side of the galaxy disc. The background level of both these stars seems to be closer to 1758 ADU, as in this case they overlap the PSFs of stars 1 and 2. The background values are low, even though both stars lie directly on top of a tidal stream. Both PSFs are markedly fainter if the value 1760 ADU is used instead.

The PSFs of stars 1 and 2 overlap each other closely for $r < 70''$. For larger radii the surface-brightness slope is positive; the overestimated measurements are there influenced by the PSF wings of other field stars as well as the varying background. The same conclusion applies as a plausible cause to the upwards slope in the outermost parts of $\mathrm{PSF_{MBH}}$. The two PSFs are about 0.5 mag arcsec^{-2} brighter than $\mathrm{PSF_{MBH}}$ at both $r = 40''$ and $r = 60''$. Their average, $\mathrm{PSF^{new}_{MBH}}$, is poorly determined for $r > 70''$. It is worth noting that the fainter parts of the surface-brightness structure of NGC 5907 depend on these far regions of the PSF.

The entire difference between $\mathrm{PSF_{MBH}}$ and $\mathrm{PSF^{new}_{MBH}}$ occurs due to a background level that is 3–4 ADU (0.17–0.23 per cent) lower than the value that MBH94 appear to use (1762–1763 ADU). This test indicates the high accuracy that is required in the background to derive a PSF with the two used relatively faint stars; it is higher than the expected accuracy of the flatfield image they use, 5–10 ADU (0.29–0.59 per cent). The data and the resulting $\mathrm{PSF^{new}_{MBH}}$ are not accurate enough to deconvolve the galaxy measurements accurately. The reconsidered $\mathrm{PSF^{new}_{MBH}}$ is also drawn in Fig. 1.

To test the influence of masking or not masking the diffraction spikes, I calculated an additional PSF where these were masked (the affected regions are indicated by the tilted cross in Fig. C.3). This test shows that the difference due to the diffraction spikes is small. The masked PSF is about 0.1 mag arcsec^{-2} fainter than the unmasked PSF at $r = 22''$, which decreases to near zero at $r = 40''$ (not shown).

For completeness, I calculated a vertical surface-brightness profile below (East-North-East of) the galaxy disc that is nearly identical to that of MBH94; to this effect I set the galaxy centre to $(x, y) = (827, 631)$ px (this position is indicated in Fig. C.1), the background value to 1760 ADU, and used the same mask. A slightly different profile results if the galaxy centre is instead set to the peak of the surface-brightness profile at $(x, y) = (827, 628)$ px. The galaxy surface-brightness structure is, moreover, not perfectly symmetric due to (horizontal) dust lanes, which are present in particular above the galaxy disc (these cannot be seen in Fig. C.1). Tidal streams above the galaxy (see fig. 2 in Martínez-Delgado et al. 2008) plausibly contribute to the asymmetry as well. The vertical profile that is measured above the disc, furthermore, differs slightly from the profile that is measured below the disc. Also, the used mask is unable to account for extended wings of the PSFs of numerous field stars around the galaxy and near the two saturated stars. However, as in the case of the two saturated stars, the biggest uncertainty to the (outer parts of the) galaxy profile is also here the background value, and the other effects are secondary to this effect. Therefore, in the discussion in Sect. 4.3 I used the profile of MBH94.

List of Objects

‘M 31’ on page 1
‘NGC 3379’ on page 1
‘A 2029’ on page 1
‘NGC 4406’ on page 1
‘NGC 4473’ on page 1
‘NGC 4550’ on page 1
‘NGC 4551’ on page 1

‘BD+30°3639’ on page 1
‘NGC 5907’ on page 2
‘the Sun’ on page 7
‘the Moon’ on page 7
‘Venus’ on page 7
‘Mars’ on page 7
‘Jupiter’ on page 7
‘Saturn’ on page 7
‘αCMa’ on page 7
‘αCar’ on page 7
‘αCen’ on page 7
‘αBoo’ on page 7
‘αLyr’ on page 7
‘αAur’ on page 7